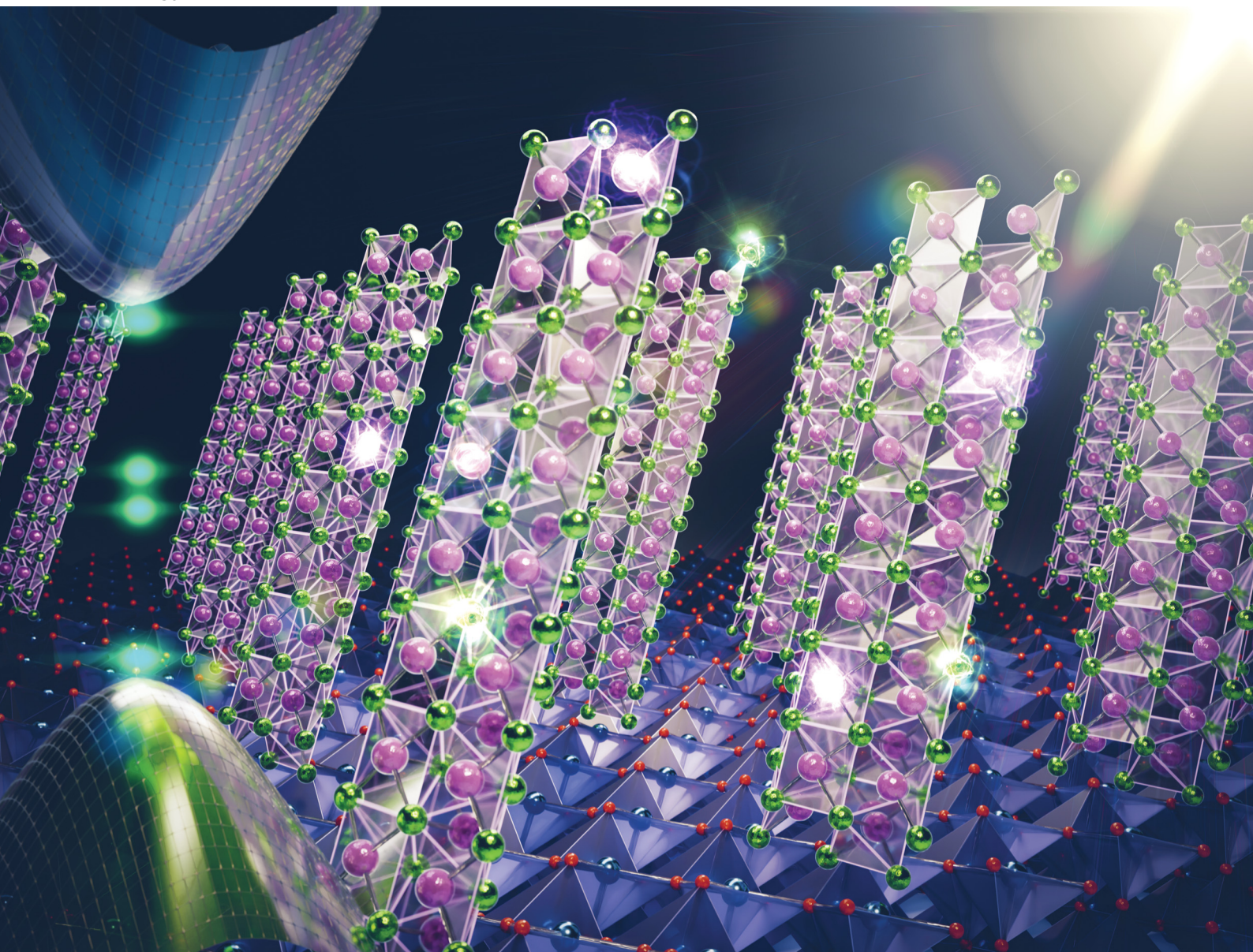


# Energy Advances

Volume 2  
Number 1  
January 2023  
Pages 1-228

[rsc.li/energy-advances](https://rsc.li/energy-advances)



ISSN 2753-1457

Cite this: *Energy Adv.*, 2023,  
2, 12Received 30th August 2022,  
Accepted 20th October 2022

DOI: 10.1039/d2ya00232a

rsc.li/energy-advances

## Defect engineering in antimony selenide thin film solar cells

Udari Wijesinghe, Giulia Longo and Oliver S. Hutter \*

Antimony selenide ( $\text{Sb}_2\text{Se}_3$ ) has gained promising attention as an inorganic absorber in thin-film photovoltaics and water splitting devices due to its excellent optoelectronic properties, low toxicity, and earth abundance. Presently,  $\text{Sb}_2\text{Se}_3$  solar cells have a record power conversion efficiency of 10.12%, with a rapid rise over the past few years. However, further efficiency increases are hindered by the severe open circuit voltage deficit associated with the defects and interfacial recombination. The existing defects impact charge carrier generation, transportation, intrinsic electrical conductivity, and film crystallinity which inevitably influences the efficiency and stability of polycrystalline  $\text{Sb}_2\text{Se}_3$  solar cells. Thus, effective defect engineering aiming at understanding the chemical nature of defects is essential to enhance the inferior performance and functional properties of  $\text{Sb}_2\text{Se}_3$  thin films. Herein, a comprehensive review of the defect chemistry at surfaces, grain boundaries, and interfaces in  $\text{Sb}_2\text{Se}_3$  solar cells, and efforts made in the community to passivate these defect states are presented. Finally, the potential challenges associated with an in-depth understanding of defect dynamics and strategies to achieve highly efficient and stable  $\text{Sb}_2\text{Se}_3$  solar cells in the future are provided.

### 1. Introduction

A globally increasing energy demand has resulted in a growing search for sustainable, reliable, and affordable photovoltaic (PV) materials. Currently, polycrystalline silicon (Si), cadmium telluride (CdTe), and copper indium gallium selenide ( $\text{Cu}(\text{In,Ga})\text{Se}_2$ , CIGS) are used as dominant absorbers in solar cells and have all achieved a certified power conversion efficiency (PCE) of over 20%.<sup>1–3</sup> However, the high processing cost of Si, the toxicity of Cd, the high price of Ga and In, and the scarcity of In, Ga, and Te is a challenging task for the mass production of thin-film solar cells from these materials.<sup>3,4</sup> Kesterite solar cells ( $\text{Cu}_2\text{ZnSn}(\text{S}_x\text{Se}_{1-x})_4$ , CZTS/Se) reached peak device efficiencies of around 12.7% in 2021.<sup>5</sup> But the rise in efficiency stagnated for years due to defects associated with the complex phase chemistry of the material. Recently, the development of halide perovskites ( $\text{CH}_3\text{NH}_3\text{PbI}_3$ ) has progressed rapidly with impressive peak device efficiencies of around 25% for perovskite materials.<sup>2</sup> However, the instability and the toxicity of lead (Pb) based perovskites drive sustained research on novel absorbers for thin-film PVs.<sup>4,6</sup>

Over the last decade, antimony selenide ( $\text{Sb}_2\text{Se}_3$ ) has gained tremendous attention in the PV regime due to a high optical absorption coefficient ( $10^5 \text{ cm}^{-1}$ ) across the visible range, a suitable

bandgap of 1.1–1.3 eV, high carrier mobility ( $10 \text{ cm}^2 \text{ V}^{-1} \text{ s}^{-1}$ ), low toxicity, simple phase chemistry, low cost, and high elemental abundance.<sup>7–11</sup> It has also yielded promising results in photoelectrochemical water splitting devices.<sup>12–15</sup> Unlike conventional absorbers,  $\text{Sb}_2\text{Se}_3$  displays a unique quasi-one-dimensional (Q1D) structure composed of  $[\text{Sb}_4\text{Se}_6]_n$  ribbons, where ribbons are held together by van der Waals forces without dangling bonds, while the Sb–Se atoms within the ribbons are covalently bonded.<sup>8,9,16</sup> However, a recent study based on first-principles calculations showed that inter-ribbon interactions in  $\text{Sb}_2\text{Se}_3$  fall between the van der Waals and covalent regime.<sup>17</sup> Other works revealed that tailoring the growth orientation of  $[\text{Sb}_4\text{Se}_6]_n$  chains closer to perpendicular to the substrate in the [211] and [221] crystal planes reduce the density of dangling bonds and create intrinsically benign grain boundaries (GBs).<sup>9,18–20</sup> Nevertheless, ribbons in the [001] plane significantly minimize non-radiative recombination losses improving the utility of  $\text{Sb}_2\text{Se}_3$  polycrystalline thin films in PVs.<sup>21,22</sup> For most known inorganic absorbers (such as Si, CIGS, and CdTe), the breakage of covalent bonds inevitably introduces defect states and recombination centers at the GBs, which can effectively block charge collection and potentially reduce device efficiency during the interface recombination. Contrastingly,  $\text{Sb}_2\text{Se}_3$  has intrinsically benign GBs which could therefore offer a sustainable solution to drawbacks associated with traditional absorber materials if efficiency values continue to rise.

$\text{Sb}_2\text{Se}_3$  is still relatively under studied compared to other technologies such as kesterite and perovskite materials.

Department of Mathematics, Physics, and Electrical Engineering,  
Northumbria University, Newcastle upon Tyne NE1 8QH, UK.  
E-mail: oliver.hutter@northumbria.ac.uk





Fig. 1 (a) The number of publications regarding  $\text{Sb}_2\text{Se}_3$  thin-film solar cells and defects analysis of  $\text{Sb}_2\text{Se}_3$  thin-film solar cells from 2015 to 2022 (data extracted from Web of Science). (b) Peak reported single junction efficiencies for different absorber materials in comparison to the S–Q limit.

To illustrate this, Fig. 1(a) provides a statistical analysis of publications related to  $\text{Sb}_2\text{Se}_3$  solar cells between 2015 and 2022. Three main areas of research within the field currently are control of the orientation of  $\text{Sb}_2\text{Se}_3$  films,<sup>9,18–20</sup> band alignment optimization,<sup>23–29</sup> and defect passivation at interfaces/surfaces to suppress recombination losses and the open circuit voltage ( $V_{\text{OC}}$ ) deficit.<sup>30–36</sup> Despite the excellent properties of  $\text{Sb}_2\text{Se}_3$ , PCEs values are still far below the maximum theoretical value of 30% predicted by the Shockley–Queisser (S–Q) model (Fig. 1(b)).<sup>37</sup> Spectroscopic limited maximum efficiency (SLME) calculations show that  $\text{Sb}_2\text{Se}_3$  has great room for development of highly efficient solar cells with an upper limit of 30%, which is actually higher than both CdTe and CZTS/Se.<sup>38</sup> Different physical and chemical techniques have been employed to fabricate  $\text{Sb}_2\text{Se}_3$  solar cells with high crystallinity that are essential to enhance conductivity, carrier separation and stability,<sup>7,9,18,21,35,39–49</sup> and PCEs have rapidly risen from 0.66% in 2009 to over 9.2% in 2019,<sup>10,18,21,35,39,50–52</sup> with highest recorded efficiency of 10.12% in 2022.<sup>53</sup>

Peak  $\text{Sb}_2\text{Se}_3$  PCEs are critically confined by a large  $V_{\text{OC}}$  deficit ( $E_{\text{g}}/q - V_{\text{OC}}$ , where  $E_{\text{g}}$  is the optical bandgap of the  $\text{Sb}_2\text{Se}_3$ , and  $q$  is the elementary charge), which is far beyond the estimated losses according to the S–Q limit (0.24–0.28 V) for a band gap range from 1.0 to 1.7 eV.<sup>54,55</sup> Moreover, there is a conspicuous gap in studies on the origins of  $V_{\text{OC}}$  losses and defect analysis of thin films (Fig. 1(a)). This is due to the defect chemistry of  $\text{Sb}_2\text{Se}_3$  being complex, and fundamental features such as carrier mobility, carrier lifetime, diffusion length, defect depth, defect density, and band tailing being mostly unexplored. Compared to  $\text{Sb}_2\text{Se}_3$ , the higher band gap sulfide analogue ( $\text{Sb}_2\text{S}_3$ ) and its alloys  $\text{Sb}_2(\text{S,Se})_3$  also exhibit similar advantages, and the disadvantage of a large  $V_{\text{OC}}$  deficit for champion devices.<sup>56,57</sup> Reported efficiencies of  $\text{Sb}_2\text{S}_3$  and  $\text{Sb}_2(\text{S,Se})_3$  solar cells are still relatively low, encountering the problem of high resistivity of the absorber, low charge extraction from the absorbing layer to the buffer layer, and easy formation of point defects deep inside the

bandgap that act as electron–hole non-radiative recombination centers.<sup>58,59</sup> Thorough understanding is lacking because of three difficulties: (i) low electrical conductivity ( $10^{-6}$ – $10^{-7}$  S  $\text{cm}^{-1}$ ) in  $\text{Sb}_2\text{Se}_3$  film leads to difficulty in analyzing carrier density and mobility directly from the Hall effect,<sup>7,10,40,60</sup> (ii) extremely limited band-to-band recombination which makes challenging the study of carrier lifetime and defect information from photoluminescence (PL),<sup>40,61</sup> (iii) strong anisotropy which renders mobility measurements very complicated.<sup>21,40,55,62</sup> In addition, defect analysis has been assessed based on the determining carrier type in the absorber, although the results are typically from a single group and often inconclusive. In most studies, it is assumed that the  $\text{Sb}_2\text{Se}_3$  absorber is predominantly p-type without determining the minority carrier type.<sup>63–66</sup> On the basis of Hall effect measurements, cyclic voltammetry, deep-level transient spectroscopy (DLTS), and X-ray photoelectron spectroscopy (XPS) analysis reported that  $\text{Sb}_2\text{Se}_3$  films show p-type character.<sup>10,31,39,67</sup> Whereas Hobson *et al.* revealed unintentional introduction of chlorine (Cl) impurities present in the purchased source material formed n-type  $\text{Sb}_2\text{Se}_3$  absorber.<sup>36</sup> Furthermore, due to the presence of extrinsic dopants such as iodine (I)<sup>44,68</sup> and tellurium (Te),<sup>32,69–71</sup> the possibility of formation of n-type devices with high efficiencies also exists. Hence, it's vitally important to consider the source of the  $\text{Sb}_2\text{Se}_3$  material and any impurities that may be present in the growth or processing environment, as  $\text{Sb}_2\text{Se}_3$  in solar cells can behave as both p-type or n-type absorbers. However, the n-type character remains less explored in the area of thin film  $\text{Sb}_2\text{Se}_3$  PVs and many other groups may well be fabricating highly efficient devices where the  $\text{Sb}_2\text{Se}_3$  can be unknowingly n-type. Therefore, the actual carrier type of  $\text{Sb}_2\text{Se}_3$  is not ambiguously clear, and the assumption of  $\text{Sb}_2\text{Se}_3$  as a p-type material without experimental validation might result in erroneous defect physics.

Defects are unavoidable in thin film fabrication, and these affect the charge carriers transport, lifetime, recombination rate, the carrier concentrations tuning, doping limit, and Fermi level for realizing the functionality of the material (*i.e.*, p-type



and n-type). The defects can form intrinsically (*i.e.*, vacancies: by the presence of missing atoms; self-interstitials: added atoms in between expected atoms position; antisites: exchanged atoms in the crystal structure) or extrinsically (*i.e.*, by the presence of foreign atoms in the crystal structure). The dislocation of atoms from the native lattice creates electronic states inside the band gap. In general, defects with low formation energies imply easy formation. The defects formed within a few  $k_B T$  ( $\sim 0.025$  eV at 300 K, where  $k_B$  is Boltzmann constant and  $T$  is temperature) from the conduction band minimum (CBM) usually act as shallow donors, whereas defects closer to valence band maximum (VBM) generally act as shallow acceptors. If the defect state is sufficiently shallow, it will readily ionize, transferring the electrons/holes to the CBM/VBM or to defect levels closer to CBM/VBM at room temperature. For easy reference, the energy levels of  $\text{Sb}_2\text{Se}_3$  are summarized in Fig. 2(a). In contrast, defects that introduce levels deep in the bandgap with energy much higher than  $k_B T$  form deep level defects (Fig. 2(b))<sup>32,39,72,73</sup> The trap states associated with deep defects usually act as detrimental traps for photo-generated carriers and act as recombination centers and dictate carrier mobility, which ultimately affects the efficiency of the device; thus, the formation of these should be avoided. Fig. 2(b) shows a simplified version of these defect levels, which does not take into account the possibility of defects changing energy through lattice relaxation upon charge capture.<sup>74</sup>

In order to characterize and provide useful information on the trap states and defects in  $\text{Sb}_2\text{Se}_3$ , computational studies such as first-principles calculations,<sup>30</sup> hybrid density functional theory (DFT),<sup>75–78</sup> and various experimental detection techniques are used. Time-resolved transient absorption (TRTA) spectroscopy is used to identify the dynamics of photogenerated carriers and defect density states of the absorber.<sup>7,79,80</sup> Temperature-dependent dark conductivity and thermal admittance spectroscopy (TAS) can determine the depth and density

of defect states.<sup>7,40</sup> DLTS,<sup>36,39</sup> capacitance–voltage ( $C-V$ ),<sup>19</sup> and capacitance–frequency ( $C-F$ )<sup>7,80</sup> are used to measure dopant concentration distribution in the absorber and to differentially identify interfacial defects from bulk defects. Furthermore, recombination mechanisms and related defects in an absorber are directly characterized through PL spectroscopy.<sup>43,81</sup> Lastly, deep level capacitance profiling (DLCP) is used to analyze minority-carrier traps in the absorber by measuring capacitance changes with voltage pulses as a function of temperature.<sup>19,40</sup>

Herein, this article provides an essential insight into defects associated with absorber surface, GBs, and interfaces and their impact on  $\text{Sb}_2\text{Se}_3$  device performance. Moreover, recent achievements and techniques used to suppress the defect states and  $V_{OC}$  issues, including passivation of point defects, post-treatments, surface modifications, and interfacial modifications, are presented. Finally, we provide current challenges and future research directions for defect control of  $\text{Sb}_2\text{Se}_3$  solar cells for further improvement of PV performance.

## 2. Defect chemistry of antimony selenide thin films

Defect tolerance (*i.e.* when no deep level defects are formed in the bandgap) is a highly desirable characteristic of a PV absorber.<sup>82,83</sup> Unintentional defects present in thin film absorbers often degrade the physicochemical and photoelectrical properties of PV devices.<sup>3,30,75</sup> Having simple binary phase chemistry,  $\text{Sb}_2\text{Se}_3$  was initially expected to have simple intrinsic point defects with benign defect properties, and defect control should have therefore been much easier than that in quaternary compounds such as CZTS/Se.<sup>6,78</sup> As such, it was expected to have six possible point defects. These are (i) two vacancies (cation vacancy,  $V_{\text{Sb}}$ , and anion vacancy,  $V_{\text{Se}}$ ). (ii) Two interstitials (cation interstitial,  $\text{Sb}_i$ , and anion interstitial,  $\text{Se}_i$ ). (iii) Two substitutions (cation-replace-anion

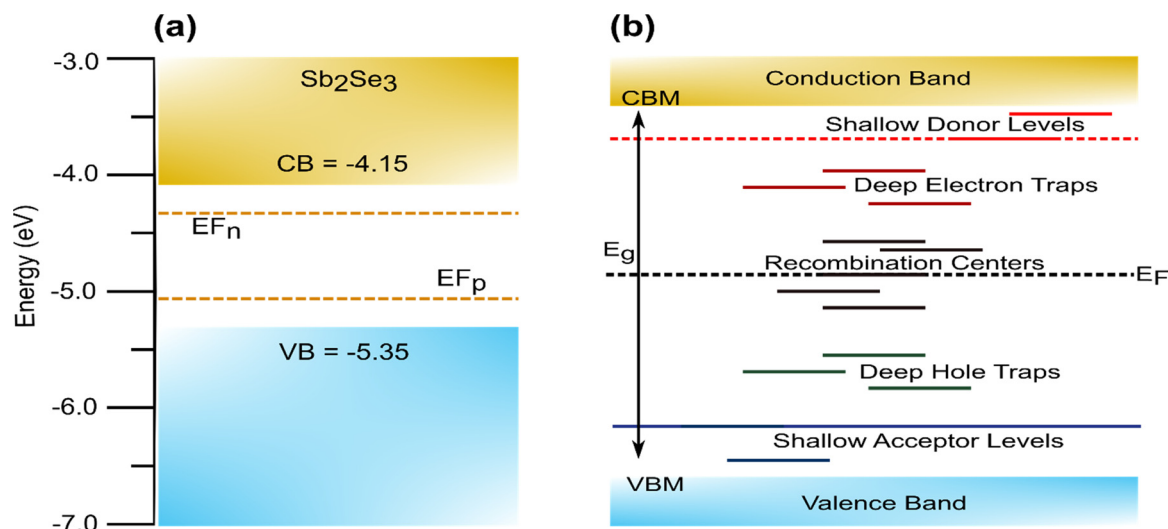


Fig. 2 (a) Schematic band structure of  $\text{Sb}_2\text{Se}_3$  with electron and hole quasi Fermi level ( $E_{F_n}$  and  $E_{F_p}$ ). (b) Simplified schematic band diagram with different defect states in a typical semiconductor material.



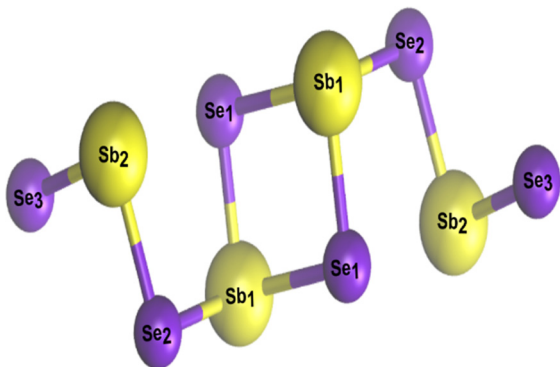


Fig. 3 Non-equivalent atomic sites in  $[Sb_4Se_6]_n$  atomic chain.

antisite,  $Sb_{Se}$ , and anion-replace-cation antisite,  $Se_{Sb}$ ).<sup>30,78,84</sup> However, the experimental and theoretical results have demonstrated that intrinsic defects in  $Sb_2Se_3$  are unexpectedly complicated and unconventional, and the defect physics in this Q1D van der Waals system cannot be simply adopted from those in the three-dimensional covalent binary PV absorbers such as GaAs and CdTe (where all the cation/anion sites remain identical).<sup>3,30,55,75</sup> This is mainly for two reasons. Firstly, due to the low symmetry of the Q1D structure, identical defects located on non-equivalent atomic sites can exhibit very different defect properties, *i.e.*, a single  $Sb_2Se_3$  ribbon shows three nonequivalent Se atomic sites ( $Se_1$ ,  $Se_2$ , and  $Se_3$ ) and two Sb atomic sites ( $Sb_1$  and  $Sb_2$  in Fig. 3). Therefore, defects associated with different atomic sites can be very different. Secondly, due to the weak van der Waals interactions between  $[Sb_4Se_6]_n$  ribbons, large voids present between different  $[Sb_4Se_6]_n$  atomic chains create uncommon defects which are difficult to form in conventional absorbers, *e.g.*, cation-replace-anion antisite ( $Sb_{Se}$ ), anion-replace-cation antisite ( $Se_{Sb}$ ), and even two-anion-replace-one-cation antisite ( $2Se_{Sb}$ ). Therefore, although there are only a few types

of point defects, the properties of these point defects are complicated by structural freedom.

As previously mentioned, crystalline defects can be broadly divided into two main categories called intrinsic and extrinsic defects. Furthermore, based on their dimensions, defects are categorized as point defects (0D), linear defects (1D), interfacial/planar defects (2D), and bulk/volume defects (3D).<sup>3,73,85</sup> All these types of defects can coexist and interact in various ways and one of these defects can then dominate to change the properties of  $Sb_2Se_3$  films, whereas others could be trivial.<sup>30,85</sup> The fabrication approach is mainly responsible for the density and the type of defects regardless of different device configurations (n-p or n-i-p or n-n). The following section discusses the experimental and theoretical findings of intrinsic and extrinsic defects in  $Sb_2Se_3$  thin films and their intrinsic behavior towards solar cells' conductivity and  $V_{OC}$  deficit.

Before entering into the details of defect formation and behavior in  $Sb_2Se_3$ , it is important to briefly explain some fundamental concepts that will be largely used in this review. Firstly, it is worth stressing the difference in meaning between “formation energy”, “transition/activation energy” and “ionization energy” of defects. Formation energy describes the Gibbs free energy necessary for the formation of defects. The lower it is, the easier it is for defects to form, and consequently they will exist in higher concentration. The “transition/activation energy” refers to the position of the traps with respect to the conduction and valence bands ( $E_{CBM} - E_T$  for electron traps and  $E_T - E_{VBM}$  for hole traps, where  $E_T$  is the energy level of defect,  $E_{CBM}$  is the energy of CBM, and  $E_{VBM}$  is the energy of VBM). The lower the activation energy, the easier it is to de-trap trapped charges. Finally, the “ionization energy” is the energy required for the trap to reduce or oxidize.

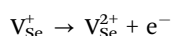
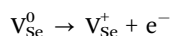
Defects can be neutral or ionized. The doping and trapping effect of charged defects is depicted in Fig. 4. If an anion with energy levels close to the CBM is introduced in the material it will likely enhance the electron concentration, acting as an n-



Fig. 4 Schematic illustration of Fermi level position ( $E_F$ ), donor, and acceptor ionization energy levels within the band gap ( $E_g$ ) of different type of absorbers (a) intrinsic absorber, (b) n-type absorber, and (c) p-type absorber.



dopant and increasing the Fermi level of the material. If the energy levels introduced by this anion are located in the middle of the bandgap or, even worse, close to the VBM, it would then annihilate holes, acting as an electron trap. The opposite would happen for cations with p-doping/electron trapping effect. However, the effect of neutral defects, especially intrinsic, can be more challenging to understand, and need careful characterization. A vacancy of selenium  $V_{Se}$ , for example, corresponds to a missing  $Se^0$  atom. This means that the electrons shared between the Sb–Se, which would naturally be localized around the more electronegative Se, are now less bounded and available to be promoted in the conduction band. For this to happen, the neutral vacancy is ionized:



A  $V_{Se}$  defect then acts as a donor, provided that the ionization energy of  $\sim 0.53$  eV for this process to happen in equilibrium conditions.<sup>76,86</sup>

## 2.1. Intrinsic defects

The high  $V_{OC}$  deficit of devices fabricated using intrinsic  $Sb_2Se_3$  is known to be one critical limitation to the performance of  $Sb_2Se_3$ -based solar cells. Currently, the best performing  $Sb_2Se_3$  solar cells have a deep defect density of  $10^{14}$ – $10^{15}$   $cm^{-3}$ , which is much higher than those in CdTe solar cells ( $10^{11}$ – $10^{13}$   $cm^{-3}$ ).<sup>18,39,87</sup> Moreover, the free carrier concentration of undoped  $Sb_2Se_3$  being limited to  $\sim 10^{13}$   $cm^{-3}$  confirms that a high concentration of defects exists in the un-ionized form.<sup>7,87</sup> To understand the correlation between defect-assisted recombination and  $V_{OC}$  loss, intrinsic point defects have been studied by first-principles calculation and DFT studies.<sup>30,75,77,78</sup> The defect formation energies of all the non-equivalent sites of  $V_{Se}$  (Se vacancy),  $V_{Sb}$  (Sb vacancy),  $Se_i$  (Se interstitial),  $Sb_i$  (Sb interstitial),  $Se_{Sb}$  (Se replace Sb antisite), and  $Sb_{Se}$  (Sb replace Se antisite) were calculated under the Se-rich and Se-poor conditions (Fig. 5(a) and (b)).<sup>30,75,78,84</sup>

**2.1.1. Se-rich conditions DFT calculations.** Liu *et al.* revealed that  $Se_{Sb}$  antisites and  $Se_i$  (non-ionized) behave as shallow acceptors (p-type) in Se-rich environment (Fig. 5(a)).<sup>78</sup> In most conventional thin-film PVs, anion-replacement antisite



Fig. 5 The calculated formation energy of point defects in  $Sb_2Se_3$  as a function of the Fermi level under (a) Se-rich condition and (b) Se-poor condition.<sup>78</sup> Defect transition-level diagrams for  $Sb_2Se_3$  under limiting chemical potential conditions (c) Se-rich condition and (d) Se-poor condition, plotting defect formation energy (eV) against the position of the Fermi level above the VBM.<sup>75</sup> (e) Transition energy levels of intrinsic defects in the bandgap of  $Sb_2Se_3$ . Red-colored levels and blue-colored levels indicate acceptor-type and donor-type defects, with their possible ionization states written above.<sup>30</sup>



defects are reported as donor defects, *i.e.*, more valence electrons around the anion than the cation, and these extra electrons can be donated. Moreover, these defects were found to have high formation energies and formed in very low concentrations, and thus their influence on the performance of the device is considered negligible.<sup>88,89</sup> Fascinatingly, the behavior of  $\text{Se}_{\text{Sb}}$  antisite defects is different in  $\text{Sb}_2\text{Se}_3$  compared to other PV materials. In fact,  $\text{Se}_{\text{Sb}}$  antisites defect behave as an acceptor defect. This can be understood thinking that when one Sb atom is replaced by a Se atom, the surrounding three Se atoms cannot get three electrons from Sb to make their 4p states fully occupied. However, the replaced Se having four 4p electrons (with similar 4p electrons energy to surrounding Se atoms) forms three covalent Se–Se bonds making the two bonding states of the p–p hybridization fully occupied. The remaining 4p electron in an antisite Se will occupy one low-energy antibonding state of the p–p hybridization, producing a singly occupied defect level in the band gap just above VBM. Since two electrons can occupy the antibonding level, this defect level can still accept an electron, making the  $\text{Se}_{\text{Sb}}$  acceptor defect. Additionally, while in conventional PV anion-replace-cation defects have generally high formation energy (and are hence scarcely present), a concentration of  $10^{14}$ – $10^{17}$   $\text{cm}^{-3}$  of  $\text{Se}_{\text{Sb}}$  defects were found in  $\text{Sb}_2\text{Se}_3$  films and were responsible for the majority of carrier concentration in multiple computational and experimental studies.<sup>30,32,39,78,84</sup> Interestingly, Huang *et al.* showed that defect complexes,  $2\text{Se}_{\text{Sb}}$  antisites (two Se anions to take the place of one Sb cation site), are favorably formed in  $\text{Sb}_2\text{Se}_3$  and have very low formation energy (Fermi level is  $<0.5$  eV above VBM).<sup>30</sup> The large structural distortion caused by two Se atoms replacing Sb is tolerated by the structural freedom between the  $[\text{Sb}_4\text{Se}_6]_n$  chains, which allows  $2\text{Se}_{\text{Sb}}$  to be present in high concentrations ( $10^{13}$ – $10^{17}$   $\text{cm}^{-3}$ ) under Se-rich conditions. Both  $2\text{Se}_{\text{Sb}}$  ( $2\text{Se}_{\text{Sb}_1}$  and  $2\text{Se}_{\text{Sb}_2}$ ) behave as acceptor defects and are dominantly present over all acceptor defects, rendering undoped  $\text{Sb}_2\text{Se}_3$  intrinsically p-type (holes are majority carriers).<sup>30,78</sup> Although defect evaluations by Savory *et al.* showed general similarity in expectations and results, some disagreement with previous results was noticed. Savory *et al.* revealed both  $\text{Se}_{\text{Sb}}$  defects are amphoteric, lying in the ultra-deep inside the band gap, which primarily acts as recombination centers and has similar potential for both electrons and holes, thus are highly detrimental to solar cell performance.<sup>75</sup>

Similarly, under Se-rich conditions, the  $\text{Se}_i$  defect was predicted *via* DFT to be present in high concentrations.<sup>75,78</sup> However, the ionization level of  $\text{Se}_i$  is above the CBM, and it does not induce any transitional levels in the bandgap (Fig. 5(e)). Therefore,  $\text{Se}_i$  influence on the PV performance is not significant and does not contribute to the carrier concentration or act as a non-radiative recombination center.<sup>78</sup> In contrast, Savory *et al.* showed  $\text{Se}_i$  has multiple transition levels deep within the band gap that could plausibly act as hole or electron traps (Fig. 5(c)).<sup>75</sup> This is contradiction to DFT calculations, showing the importance of corroborating theoretical findings with experimental results. It also predicted that under a Se-rich environment,  $\text{V}_{\text{Sb}}$  acts as an acceptor with transition

levels lying 0.15 eV above the VBM at a neutral state, and when ionized, the Fermi energy shifts to the CBM vicinity (Fig. 5(a) and (e)).<sup>30,75</sup> The formation enthalpy of  $\text{V}_{\text{Sb}}$  becomes negative as the Fermi level approaches the CBM, thus limiting the Fermi level rising further. Thus, observed p-type conductivity cannot result from  $\text{V}_{\text{Sb}}$ . In addition, donor defects  $\text{V}_{\text{Se}_2}$  and  $\text{V}_{\text{Se}_3}$ , produce at deep levels in the band gap and act as effective recombination centers for  $\text{Sb}_2\text{Se}_3$ .<sup>30,84</sup> The acceptor defects  $\text{Se}_{\text{Sb}_2}$  and  $2\text{Se}_{\text{Sb}_2}$ , which have lower formation energies and produce higher concentrations of hole carriers, make undoped  $\text{Sb}_2\text{Se}_3$  thin films intrinsically p-type under Se-rich conditions.

**2.1.2. Se-poor conditions DFT calculations.** On the other hand, under the Se-poor regime, the formation energies of acceptor defects such as  $\text{Se}_{\text{Sb}_1}$  and  $\text{Se}_{\text{Sb}_2}$  increase significantly with consequently lower formation probability ( $>1$  eV) while all the donor defects formation energies decrease ( $\text{V}_{\text{Se}}$  and  $\text{Sb}_{\text{Se}}$ ) and easily form. All anion vacancies ( $\text{V}_{\text{Se}_1}$ ,  $\text{V}_{\text{Se}_2}$ , and  $\text{V}_{\text{Se}_3}$ ) are donor defects, and  $\text{V}_{\text{Se}_2}$  and  $\text{V}_{\text{Se}_3}$  (which have the lowest formation energies among all the donor defects), contribute more to electron carrier concentration in  $\text{Sb}_2\text{Se}_3$  films.<sup>30,78,84</sup> However, Liu *et al.* revealed despite the low formation energy,  $\text{V}_{\text{Se}}$  is hard to ionize as these defects lie very deep in the bandgap at the neutral state.<sup>78</sup> Therefore, the amount of ionized  $\text{V}_{\text{Se}}$  defects is very low, which means that also their contribution to free electrons is limited. Furthermore, at charged states,  $\text{Sb}_{\text{Se}_2}$  and  $\text{Sb}_{\text{Se}_3}$  reside close to the middle of the band gap, whereas  $\text{Sb}_{\text{Se}_1}$  is closer to the VBM level, which results in deep donor defects effects similar to  $\text{V}_{\text{Se}}$  (Fig. 5(e)).<sup>30,77</sup> Thus, Se-poor samples show intrinsic character or weak n-type conductivity with a low carrier concentration as the Fermi level is located near the middle of the bandgap. Under this condition, Huang *et al.* showed donor defects  $\text{Sb}_{\text{Se}_2}$ ,  $\text{Sb}_{\text{Se}_3}$ ,  $\text{V}_{\text{Se}_2}$ , and  $\text{V}_{\text{Se}_3}$  are prone to produce deep levels and will act as effective recombination centers in n-type  $\text{Sb}_2\text{Se}_3$ .<sup>30,84</sup> Contradictory DFT calculations carried out by Savory *et al.* depict that regardless of the site, all the three  $\text{V}_{\text{Se}}$  act as deep donors and all  $\text{Sb}_{\text{Se}}$  ( $\text{Sb}_{\text{Se}_1}$ ,  $\text{Sb}_{\text{Se}_2}$ ,  $\text{Sb}_{\text{Se}_3}$ ) as amphoteric defects, which can be possible trap states for both electrons and holes (Fig. 5(d)).<sup>75</sup> Overall results show that the formation of an intrinsic n-type absorber is unlikely because  $\text{V}_{\text{Se}}$  and  $\text{Sb}_{\text{Se}}$  restrain the Fermi level from reaching the CBM in Se-poor environment. A summary of intrinsic  $\text{Sb}_2\text{Se}_3$  defects under Se-rich and Se-poor environments obtained from DFT analysis are listed in Table 1.

**2.1.3. Experimental evaluation of intrinsic defects.** To date, comprehensive experimental studies have been carried out by several groups using DLTS, TAS, PL, and temperature-dependent dark conductivity.<sup>7,39,80,90</sup> Recently, Wen *et al.* carried out a DLTS analysis on  $\text{Sb}_2\text{Se}_3$  films produced by vapor transport deposition (VTD) and rapid thermal deposition (RTE).<sup>39</sup>

DLTS measures the activation energy for carrier emission from a defect (Fig. 6(a)). In DLTS spectra, positive peaks represent minority-carrier traps corresponding to electron traps, while negative peaks indicate hole traps. In both cases, two hole traps and one electron trap appeared in similar positions, albeit with different densities. Considering VTD, two hole traps at energy levels of 0.48 eV and 0.71 eV above



**Table 1** Summary of theoretically evaluated intrinsic defects in  $\text{Sb}_2\text{Se}_3$  thin films. (Here, activation energy is the  $E_{\text{VBM}}/E_{\text{CBM}} \pm E_{\text{T}}$ , the energy level of the defect in the bandgap away from VBM/CBM)

Se-rich					Se-poor			
Defect	Type of defect	Formation energy (eV)	Activation energy (eV)	Ref.	Type of defect	Formation energy (eV)	Activation energy (eV)	Ref.
$\text{Se}_{\text{Sb}}$	Shallow acceptor	0.60	$E_{\text{VBM}} + 0.12$	78	—	> 1	—	78
	Amphoteric	< 1.5	$E_{\text{VBM}} + 0.69$	75	—	> 1	—	78
	Acceptor	< 1	$E_{\text{VBM}} + > 0.40$	30	—	> 1	—	78
$2\text{Se}_{\text{Sb}}$	Shallow acceptor	—	—	30	—	> 1	—	78
$\text{Se}_{\text{i}}$	Shallow acceptor	0.60	—	78	—	> 1	—	78
$\text{Sb}_{\text{Se}}$	Donor	—	$E_{\text{VBM}} + 0.49$	75	Deep donors	< 1	$E_{\text{CBM}} - 0.77$	78
	—	—	—	—	Deep donor	< 1	$E_{\text{CBM}} - 0.30$	30
	—	—	—	—	Amphoteric	< 1.5	$E_{\text{VBM}} + 0.58$	75
$\text{V}_{\text{Se}}$	Donor	1.1	$\text{V}_{\text{Se}_1}: E_{\text{VBM}} + 0.20, \text{V}_{\text{Se}_2}: E_{\text{VBM}} + 0.80, \text{V}_{\text{Se}_3}: E_{\text{VBM}} + 0.65$	30 and 84	Deep donors	< 1	$E_{\text{CBM}} - 0.74$	78
					Deep donors	< 1.5	$E_{\text{VBM}} + 0.58$	75
					Deep donor	< 1	$E_{\text{CBM}} - 0.30$	30
$\text{V}_{\text{Sb}}$ $\text{Sb}_{\text{i}}$	Deep acceptor	> 1.5	$E_{\text{VBM}} + 0.62$	75	Donor	< 1.5	—	75

the VBM occurred, while an electron trap was identified at 0.61 eV below CBM (Fig. 6(b)). That study attributed hole traps (acceptor defects) to  $\text{V}_{\text{Sb}}$  and  $\text{Se}_{\text{Sb}}$ , whereas electron traps (donor defects) corresponded to  $\text{Sb}_{\text{Se}}$ . Meanwhile,  $\text{Sb}_2\text{Se}_3$  solar cells fabricated by RTE also display the same point defects corresponding to  $\text{V}_{\text{Sb}}$  and  $\text{Se}_{\text{Sb}}$  at 0.49 eV and 0.74 eV from VBM and  $\text{Sb}_{\text{Se}}$  with 0.60 eV below the CBM (Fig. 6(c)). These results are consistent with the DFT results of Savory *et al.*<sup>75</sup> VTD- $\text{Sb}_2\text{Se}_3$  films have proved to have a reduced trap concentration of  $10^{14} \text{ cm}^{-3}$  (compared  $10^{15} \text{ cm}^{-3}$  in RTE- $\text{Sb}_2\text{Se}_3$  films) and a long carrier lifetime of 1339 ps (compared 1149 ps for RTE- $\text{Sb}_2\text{Se}_3$  film). Moreover, VTD films were shown to form  $\text{Se}_{\text{Sb}}$  and  $\text{Sb}_{\text{Se}}$  in similar defect densities ( $\text{Se}_{\text{Sb}}; N_{\text{T}} = 1.1 \times 10^{14} \text{ cm}^{-3}$  and  $\text{Sb}_{\text{Se}}; N_{\text{T}} = 2.6 \times 10^{14} \text{ cm}^{-3}$ ). This shows the possibility of the formation of  $\text{Sb}_{\text{Se}}$  and  $\text{Se}_{\text{Sb}}$  antisite defect pairs in  $\text{Sb}_2\text{Se}_3$  films, presumably forming  $[\text{Sb}_{\text{Se}} + \text{Se}_{\text{Sb}}]$  defect complexes. Thus, complex defect pairs would influence the shift of quasi-Fermi levels, cause serious non-radiative recombination, and lessen the  $V_{\text{OC}}$  and device efficiency.<sup>30,39,55</sup> DLTS showed that the activation energy of  $\text{Sb}_{\text{Se}}$  in p-type samples lays between 0.50–0.65 eV,<sup>91</sup> which is higher than those predicted by DFT.<sup>77</sup> In TAS analysis, three defect levels within the bandgap were detected for  $\text{Sb}_2\text{Se}_3$ , ranging from 0.2 to 0.6 eV.<sup>90,92</sup> Hu *et al.* systematically analyzed three defects located in the ranges of 0.3–0.4 eV, 0.2–0.6 eV, and 0.5–0.6 eV above the VBM, which were indicated as D1, D2, and D3, respectively<sup>90</sup> using temperature dependent TAS. However, TAS analysis failed to distinguish the nature of these defects, (*i.e.*, electron or hole traps). This serves as a good example of where DFT calculations could be better utilized to explain the experimental results.

Furthermore, TAS analysis determined a single defect state presiding with activation energy of 0.095 eV in RTE fabricated  $\text{Sb}_2\text{Se}_3$  films with  $N_{\text{T}}$  of  $1.3 \times 10^{15} \text{ cm}^{-3}$ . In contrast, temperature-dependent conductance analyzed two defects with activation energies of 0.578 eV and 0.111 eV.<sup>7</sup> Accordingly to theoretical calculations, defects with the lowest activation energy of 0.111 eV are ascribed to the  $\text{Se}_{\text{Sb}}$ .<sup>30</sup> This shows that  $\text{Se}_{\text{Sb}}$  is a shallow acceptor with a defect depth of 0.1 eV above

the VBM, and thus contributes to p-type conductivity in films. On the other hand, similar to Liu *et al.*<sup>78</sup> Zeng *et al.* reported that  $\text{V}_{\text{Se}}$  is an n-type donor that effectively reduces the p-type conductivity but also behaves as a recombination center for the photo-generated carriers on films.<sup>16</sup> This makes it important to control the formation of  $\text{V}_{\text{Se}}$  to enhance solar cell performance. A study by Grossberg *et al.* identified three bands at 0.94, 1.10, and 1.24 eV with small thermal energies of 0.033, 0.065, and 0.093 eV, respectively (Fig. 6(d)).<sup>81</sup> The PL bands at 1.24 eV and 0.94 eV were thought to originate from donor–acceptor defect pair recombination.<sup>93</sup> The 1.24 eV band results from more distant donor–acceptor pairs (shallowest single acceptor defect  $\text{Se}_{\text{Sb}}$  formed at a depth of about 0.1 eV). The 0.94 eV band originates from deep donor–deep acceptor recombination, where the donor and acceptor defects occupy the closest Se and Sb sites in the lattice ( $\text{Sb}_{\text{T}}\text{-Se}_3$  sites). The third PL band at 1.10 eV is proposed to be related to the GBs; still, further studies are needed to clarify the recombination model.<sup>81</sup> The intrinsic defect information of  $\text{Sb}_2\text{Se}_3$  obtained using various detection techniques is listed in Table 2.

Overall, studies show that defect properties of the atoms on non-equivalent sites are quite different, and defect tolerance changes significantly when the defect gets ionized in different environments. Intrinsic deep defects have a lower concentration under Se-rich conditions than in Se-poor conditions, which results in longer minority carrier lifetime, and better p-type conductivity. Thus, much better PCEs can be achieved for the devices grown under Se-rich conditions. Notably, there is a difference in defect analysis between theoretical and experimental calculations. Compared to theoretical studies, only three defects were found in the DLTS, TAS, and PL experiment analysis in each  $\text{Sb}_2\text{Se}_3$  film. This is because theoretical calculations consider all possible sites and different charge states for each defect, whereas experimental methods only probe deep-level defects in the depletion region. As a result, defects that cannot be activated or ionized at room temperature or shallow-level defects are not observed. Therefore, utilizing experimental techniques often leaves significant





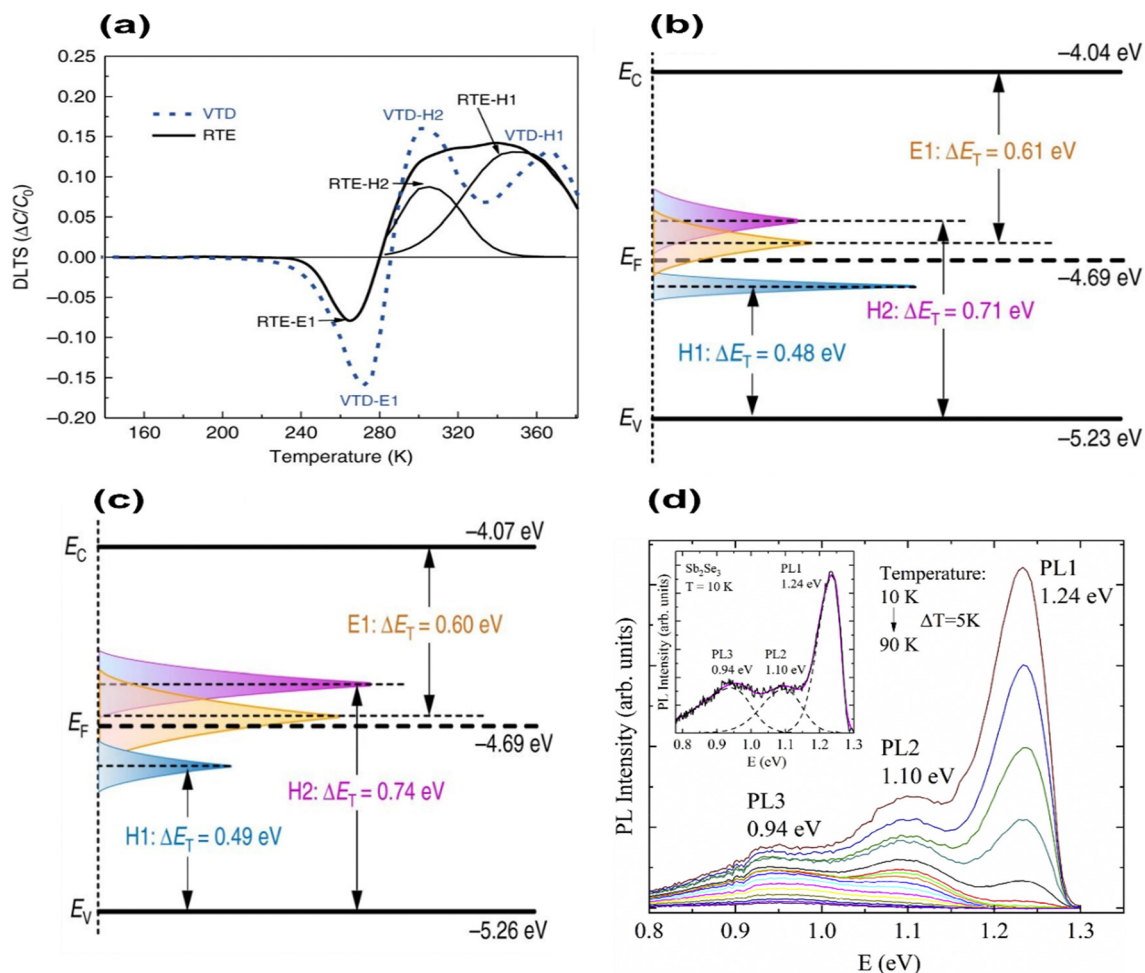


Fig. 6 Schematic of the band structure of (a) DLTS signals of VTD-fabricated and RTE-fabricated devices, (b) VTD fabricated  $\text{Sb}_2\text{Se}_3$  films, and (c) RTE fabricated  $\text{Sb}_2\text{Se}_3$  films (conduction band ( $E_C$ ), valence band ( $E_V$ ), Fermi level ( $E_F$ ), and trap energy level ( $E_T$ )).<sup>39</sup> (d) Temperature dependence of the PL spectrum of  $\text{Sb}_2\text{Se}_3$  polycrystals.<sup>81</sup>

ambiguity on which specific defect give rise to a specific signal (e.g.,  $\text{Sb}_{\text{Se}}$  or  $\text{V}_{\text{Se}}$  for Se-poor conditions), whilst also crucial as it only observes the most detrimental defects. Once more, this stress the importance of the combination of computational and experimental analysis.

## 2.2. Extrinsic defects

Extrinsic point defects can be intentionally or unintentionally introduced during the fabrication of  $\text{Sb}_2\text{Se}_3$  films. Controlling unintentional impurities is essential in solar cell fabrication as many common metal contaminants are detrimental to the PCE owing to their deep defect levels.<sup>97,98</sup> The impurities/dopants can preferentially reside in substitutional sites, replacing atoms on the crystal lattice, interstitial sites or GBs.<sup>70,99</sup> The location of these new defects within the absorber depends on dopant or impurity atomic radius, charge, and bulk crystal structure. The introduction of a dopant can induce changes to carrier density and charge carrier nature in the absorber layer, change the state of intrinsic bulk defects, or introduce new extrinsic defects. These dopants can remain as isolated point defects or join with intrinsic defects to form defect complexes leading to more

significant charge traps and defects like planar faults and voids. Under some circumstances, doping-related defects occur within the band gap in large enough concentrations to outnumber native intrinsic point defects and affect the electronic properties of the absorber. Depending on the conductivity properties, dopants can be characterized either as n-type or p-type. Different ratios of doping affect the band offsets of the absorber to form a n-p or n-i-p junction, *i.e.*, sufficient doping density is known to produce bandgap bending at the interface and slightly reduce the amplitude of the interface recombination.<sup>55,59</sup> A doping density of  $10^{13}$   $\text{cm}^{-3}$  for RTE fabricated  $\text{Sb}_2\text{Se}_3$  films (lower than that of CdTe at  $10^{14}$   $\text{cm}^{-3}$ ) and effective doping strategies with shallow depth, and small capture cross section are required for substantial improvement of hole densities or electron densities.<sup>7,35</sup> But, effective p-type doping is fundamentally difficult in  $\text{Sb}_2\text{Se}_3$  due to the presence of insufficiently shallow intrinsic point defects such as  $\text{V}_{\text{Sb}}$  and  $\text{Se}_{\text{Sb}}$ .<sup>30,100</sup> Moreover, extrinsic dopants preferentially enter into interstitial sites between ribbons rather than into the matrix, where dopants are largely inactive or act as donors leading to low p-doping efficiency and thus a low hole concentration.<sup>101-106</sup> Therefore,



Table 2 Summary of experimentally evaluated intrinsic defects in Sb<sub>2</sub>Se<sub>3</sub> thin films

Analysis method	Defect type	Assignment	Activation energy (eV)	Defect concentration ( $N_T$ ) [cm <sup>-3</sup> ]	PCE [%]	Ref.
Conductivity	Hole trap	Se <sub>Sb</sub>	0.111	$1.3 \times 10^{15}$	—	7
		—	0.578			
Conductivity	Donor	Sb <sub>Se</sub> or V <sub>Se</sub>	0.308	—	2.92	78
		—	0.518	—		
		—	0.480–0.490	$1.2 \times 10^{15}$		
DLTS	Hole trap	V <sub>Sb</sub>	0.480–0.490	$1.2 \times 10^{15}$	7.60	39
	Hole trap	Se <sub>Sb</sub>	0.710–0.740	$1.1 \times 10^{14}$		
	Electron trap	Sb <sub>Se</sub>	0.600–0.610	$2.6 \times 10^{14}$		
DLTS	Hole trap	V <sub>Sb</sub>	0.480	$6.1 \times 10^{14}$	5.40	32
		Se <sub>Sb</sub>	0.710	$1.0 \times 10^{15}$		
		Sb <sub>Se</sub>	0.630	$6.5 \times 10^{14}$		
DLTS	Electron trap	V <sub>Se2</sub>	0.390	$(0.98-1.10) \times 10^{14}$	5.60	36
		Se <sub>Sb1</sub> or V <sub>Sb1</sub>	0.460	$(4.15-8.71) \times 10^{14}$		
		V <sub>Sb2</sub>	0.690	$(1.18-2.61) \times 10^{15}$		
TAS	—	—	0.350	$1.9 \times 10^{14}$	5.74	94
		—	0.440	$6.7 \times 10^{14}$		
		—	0.610	$3.3 \times 10^{15}$		
TAS	—	—	0.490	$2.2 \times 10^{14}$	5.91	92
		—	0.350	$1.1 \times 10^{15}$		
		—	0.530	$2.5 \times 10^{15}$		
TAS	—	Bulk defects	0.360	$2.2 \times 10^{14}$	7.50	95
		Bulk defects	0.390	$6.1 \times 10^{14}$		
		Interfacial defects	0.430	$7.0 \times 10^{15}$		
TAS	Donor defects	V <sub>Se</sub>	0.450	$9.3 \times 10^{15}$	6.06	41
	Donor defects	Sb <sub>Se</sub>	0.490	$2.1 \times 10^{16}$		
TAS	Shallow acceptor	V <sub>Sb</sub>	0.180	$8.6 \times 10^{15}$	6.15	96
		Se <sub>i</sub>	0.530	$4.3 \times 10^{16}$		
TAS	Hole trap	Se <sub>Sb</sub>	0.570	$2.5 \times 10^{16}$	5.91	90
		Bulk defect	0.286	$2.4 \times 10^{14}$		
		Bulk defect	0.188	$1.3 \times 10^{15}$		
PL	Hole trap	Interface defect	0.570	$1.2 \times 10^{16}$	—	81
		—	0.330	—		
		—	0.650	—		
—	—	—	0.930	—	—	—

the effective influence of the dopants on electrochemical properties of the Sb<sub>2</sub>Se<sub>3</sub> is ambiguous, and an in-depth understanding of the mechanisms aligned with the physicochemical properties of each type of defect/defect pair is critical to interpreting the improvement of Sb<sub>2</sub>Se<sub>3</sub> thin film solar cells.

**2.2.1. Effective p-type doping.** Theoretical and experimental analysis has proved that tin (Sn) and copper (Cu) behave as p-type dopants in Sb<sub>2</sub>Se<sub>3</sub>. In the case of Sn doping, Sn was found to form a ternary Sn–Sb–Se system, *i.e.*, tetragonal (β)-Sn, SnSe<sub>2</sub>, and SnSe inside the Sb<sub>2</sub>Se<sub>3</sub> matrix, and SnSe<sub>2</sub> and SnSe phases are found to be highly thermodynamically stable in Se-rich and Se-poor environments respectively. Therefore, to avoid the formation of undesirable phases and to avoid matrix destabilization, only a trace amount of Sn (*i.e.*, Sn/Sb ratio should be low) can be sustained inside the Sb<sub>2</sub>Se<sub>3</sub> structure. The greater conductivity in Se-rich Sn-doped Sb<sub>2</sub>Se<sub>3</sub> films is due to the extrinsic acceptor substitution defect Sn<sub>Sb</sub>.<sup>76</sup> The Sn<sub>Sb</sub> was found to be located ~0.24 eV above the VBM. Sn<sub>Sb</sub> defects have low formation energy and provides a significantly greater carrier density than intrinsic Sb<sub>2</sub>Se<sub>3</sub>. This is consistent with experimental work where the addition of Sn enhanced the p-type conductivity of Sb<sub>2</sub>Se<sub>3</sub> thin films.<sup>99</sup> In Se-poor Sn-doping, Sn<sub>i</sub> formation restricts carrier mobility and/or compensates doping. This may be because the donor effect of Sn<sub>i</sub> might be hindered by the presence of higher concentrations of V<sub>Se</sub> recombination centers which are detrimental device performance.<sup>30,78</sup>

Under Se-rich conditions, both extrinsic donor Cu<sub>i</sub> and extrinsic acceptor Cu<sub>Sb1</sub> defects were stable.<sup>76,107</sup> The formation energy of Cu<sub>Sb1</sub> is lower than that of Cu<sub>Sb2</sub> and Cu<sub>Sb1</sub>, and defects formed at a transition level of 0.25 eV above the VBM. They claim that the deep level defect Cu<sub>Sb1</sub> compensated the formation of defects at high concentrations. Competition between the Cu<sub>Sb1</sub> and Cu<sub>i</sub> tends to move the Fermi level to 0.13 eV above the VBM at room temperature, allowing significant improvement of the p-type conductivity. On the other hand, in a Se-poor environment, Cu<sub>i</sub> has a much lower formation energy (0.75 eV) than Cu<sub>Sb</sub> (1.46 eV) and a Cu<sub>i</sub> donor defect formed 0.37 eV below the CBM.<sup>107</sup> Stolaroff *et al.* claim that electronically active levels are unambiguously too deep to induce any n-type doping of the absorber at room temperature.<sup>76</sup> Moreover, the formation of Cu<sub>i</sub> was compensated by the Sb<sub>Se</sub> a comparable amount, and due to this conflict, the Fermi level shifted to 0.22 eV above the VBM at room temperature, resulting in a slight enhancement of p-type conductivity. However, Chen *et al.* experimentally showed that n-type doping after copper chloride (CuCl<sub>2</sub>) chemical bath is due to formation of Cu<sub>i</sub> defects in high concentrations under Se-poor environment.<sup>107</sup>

**2.2.2. Effective n-type doping.** DFT calculations showed that Cl incorporation formed n-type Sb<sub>2</sub>Se<sub>3</sub>.<sup>36,76</sup> Stolaroff *et al.* show that the calculated formation energies for Cl<sub>Se</sub> are ~0.2 eV for both Cl<sub>Se1</sub> and Cl<sub>Se2</sub> and ~0.05 eV for Cl<sub>Se3</sub> under the CBM in Se-rich conditions. These are lower than for Se-poor



conditions.<sup>76</sup> In contrast, Hobson *et al.* revealed independently from the chemical environment,  $\text{Cl}_{\text{Se}}$  is a dominant defect, with low formation energies of  $<0.5$  eV on all Se atomic sites and occurs at a transition level of 0.025 eV closer to CBM.<sup>108</sup> The formed  $\text{Cl}_{\text{Se}}$  donor defects donate electrons to the CBM however, the concentration of  $\text{Cl}_{\text{Se}}$  will be compensated by  $\text{V}_{\text{Sb}}$  below CBM and pin the Fermi level to 0.3 eV below the CBM edge. The Cl doping produced an electron concentration of  $2.5 \times 10^{18} \text{ cm}^{-3}$  (Se-rich) or  $2.1 \times 10^{20} \text{ cm}^{-3}$  (Se-poor) and has yielded high efficient n-type  $\text{Sb}_2\text{Se}_3$  solar cells.<sup>108</sup> Furthermore, in the case of bromine (Br) and I produce three extrinsic defects where  $\text{Br}_{\text{Se}}$  ( $\text{Br}_{\text{Se}_1}$ ,  $\text{Br}_{\text{Se}_2}$ , and  $\text{Br}_{\text{Se}_3}$ ) and  $\text{I}_{\text{Se}}$  ( $\text{I}_{\text{Se}_1}$ ,  $\text{I}_{\text{Se}_2}$ , and  $\text{I}_{\text{Se}_3}$ ) substitutions are around 0.06 eV and 0.10 eV under the CBM for Br and I, respectively.<sup>76</sup> This study further showed that although the  $\text{Br}_1$  and  $\text{Br}_{\text{Se}}$  formation enthalpies remain closer,  $\text{Br}_1$  defects do not competitively form with  $\text{Br}_{\text{Se}}$  due to enthalpy hindrance, and  $\text{I}_1$  never crosses the lines formed by the formation enthalpies of  $\text{I}_{\text{Se}_{1-3}}$ . Consequently, I as a dopant seems to be the most favorable dopant for the  $\text{Sb}_2\text{Se}_3$  matrix by experimental analysis shows pinned the Fermi level towards the conduction band, which is undoubtedly the manifestation of observed n-type doping.

### 2.3. Interfacial defects of antimony selenide thin film solar cells

The discussion so far has focused on defects formed in the bulk of the material. However, interfacial defects formed between the  $\text{Sb}_2\text{Se}_3$  film and the transport layers, are also present and deserve a separate discussion. Interfacial defects of  $\text{Sb}_2\text{Se}_3$  solar cells have been studied by *C-V* and DLCP; however, substantial understanding of the origin of interfacial defects of  $\text{Sb}_2\text{Se}_3$  is still lacking.<sup>109</sup> In addition, the interfacial band alignment of each layer has been measured by ultraviolet photoelectron spectroscopy (UPS).<sup>41,67,110</sup> However, in non-pristine non-ultra-high vacuum conditions, the interfacial band alignment is largely affected by the interfacial defects and interfacial band bending.

Therefore, direct measurement of chemical state variation at interfaces and band alignments with advanced techniques such as high-resolution photoemission spectroscopy (HRPES) and XPS are required.<sup>24,111,112</sup> An ideal buffer layer should yield proper band alignment with a minimum conduction band offset (CBO), which enables stronger photocarrier transport and suppresses lattice mismatch and carrier recombination at the buffer/ $\text{Sb}_2\text{Se}_3$  interface. Cadmium sulfide (CdS), zinc oxide (ZnO), and titanium dioxide ( $\text{TiO}_2$ ) are the widely adopted buffer layers for  $\text{Sb}_2\text{Se}_3$  solar cells, and the CBO has been reported for buffer/ $\text{Sb}_2\text{Se}_3$  pairings by several groups.<sup>18,19,113</sup> The HRPES determined CBOs of CdS, ZnO, and  $\text{TiO}_2$  with  $\text{Sb}_2\text{Se}_3$  form a spike-like (positive band offset) with 0.24 eV, cliff-like band alignment with  $-0.11$  eV (negative band offset), and nearly a flat band alignment with no distinct transition layers (0 eV) respectively (Fig. 7).<sup>111</sup> On the contrary, Li *et al.* claimed that CdS/ $\text{Sb}_2\text{Se}_3$  was a  $-0.09$  eV cliff-like layout.<sup>23</sup> Further, CBO and valence band offset (VBO) determined by XPS revealed a spike of 0.25 eV and a cliff of 1.02 eV, respectively.<sup>114</sup> This shows that empirical results were inconsistent with one another, and this might be due to the variations in the surface quality of the absorber and different junction formation processes in solar cells (superstrate and substrate), making it difficult to accurately determine the band bending near the surface of the absorber. Furthermore, more advanced characterization techniques to directly measure the CBO value are required to fully identify the CBO loss.

Although high PCE values for  $\text{Sb}_2\text{Se}_3$  solar cells with CdS buffer layers have been achieved, absorption loss in the short wavelength region, and Cd/Sinterdiffusion into  $\text{Sb}_2\text{Se}_3$  film are identified as the main drawbacks. S diffusion was found to be dominant over Cd diffusion, which is responsible for the severe device degradation, causing interfacial defects (*e.g.*,  $\text{Se}_\text{S}$  and  $\text{S}_\text{Se}$ ). Furthermore, replacing  $\text{Sb}^{3+}$  sites with  $\text{Cd}^{2+}$  ions was found to decrease the p-type conductivity of  $\text{Sb}_2\text{Se}_3$ . Thus, several groups focused on modifying the CdS buffer layer by including



Fig. 7 Schematics of the band alignments between  $\text{Sb}_2\text{Se}_3$  and different buffer layers (a) CdS, (b) ZnO, and (c)  $\text{TiO}_2$ .<sup>111</sup>



doping, surface treatments, or substituting with appropriate alternatives to improve band alignment with device stability. Learning from CdTe solar cells,<sup>115</sup> doping of the CdS layer by replacing some Cd or S atoms with oxygen (O<sub>2</sub>) was applied to Sb<sub>2</sub>Se<sub>3</sub> solar cells.<sup>29</sup> Notably, the introduction of n-type O<sub>2</sub> was found to improve the n–p junction quality by suppressing the carrier recombination at the absorber/Sb<sub>2</sub>Se<sub>3</sub> interface. Moreover, doping of the buffer widens the band gap of the CdS and tunes the energy alignment from “cliff” like to “spike” like.<sup>29</sup> Similarly, Guo *et al.* reported accumulation of the O<sub>2</sub> at the CdS:O/Sb<sub>2</sub>Se<sub>3</sub>, significantly suppressing interfacial diffusion of Cd and formation of n-type Cd.<sup>116</sup> With a trace amount of Cl and more O, the surface defects on CdS grains were passivated, reducing the ideality factor (*A*) from 2.70 to 2.16 and the reverse saturation current density (*J*<sub>0</sub>) from 0.09 mA cm<sup>-2</sup> to 0.02 mA cm<sup>-2</sup> in CdCl<sub>2</sub> treated devices compared to a control device.<sup>117</sup> Furthermore, ambient storage of films decreases the *A* from 2.2 to 1.9 and the *J*<sub>0</sub> from 9.0 × 10<sup>2</sup> mA cm<sup>-2</sup> to 8.7 × 10<sup>3</sup> mA cm<sup>-2</sup>, exhibited reduced recombination loss or equivalently improved transmission and junction quality.<sup>67</sup> The isotropic O<sub>2</sub> diffusion into Sb<sub>2</sub>Se<sub>3</sub> was found to tailor the (Sb<sub>4</sub>Se<sub>6</sub>)<sub>*n*</sub> ribbons to a [221] textured orientation, forming Sb–O–Se chains or SbSeO<sub>*x*</sub> compounds, which can fill the van der Waals gap between the Q1D ribbons.<sup>118</sup> This demonstrates that O<sub>2</sub> provides a unique pathway to engineer the morphology, interface quality, electrical and optical properties as well as performance of Sb<sub>2</sub>Se<sub>3</sub> solar cells.<sup>116,118</sup> Combined analysis of *C–V* and DLCP characterization stated thermally evaporated Sb<sub>2</sub>Se<sub>3</sub> films contain interfacial traps of 10<sup>16</sup> cm<sup>3</sup> while Se compensated films contain reduced traps of 10<sup>15</sup> cm<sup>3</sup>. This revealed Se interfacial defect passivation by Se compensation is an effective method compared to O<sub>2</sub> treatment during film evaporation. However, defects associated with O, Cd, S, Sb, and Se needed to be thoroughly evaluated for the future development of PVs.

Wang *et al.* showed substrate temperature and annealing duration of ZnO produced by spray pyrolysis plays a decisive role in the crystal orientation of Sb<sub>2</sub>Se<sub>3</sub>.<sup>19</sup> It was noticed that [001]-oriented ZnO results in higher interfacial defect density of 3.77 × 10<sup>11</sup> cm<sup>-2</sup> than random orientated ZnO (1.22 × 10<sup>11</sup> cm<sup>-2</sup>). Consequently, the growth of [221]-oriented Sb<sub>2</sub>Se<sub>3</sub> films is not thermodynamically feasible on the [001] plane of ZnO due to dangling bonds and poor film adhesion. Conversely, randomly orientated ZnO always promotes [221] orientation of Sb<sub>2</sub>Se<sub>3</sub> grains.

Recently, many literature reports have revealed that desired crystal orientation with higher PCEs have been achieved in both superstrate and substrate Sb<sub>2</sub>Se<sub>3</sub> solar cells using TiO<sub>2</sub> as a buffer layer.<sup>9,20,113,119</sup> Kondrotas *et al.* revealed that bonding of Sb and Se with the TiO<sub>2</sub> substrate during the film deposition is difficult due to higher Ti–O bond energy (662 kJ mol<sup>-1</sup>) than Cd–S (196 kJ mol<sup>-1</sup>). This means that when CdS is used, most of the (Sb<sub>4</sub>Se<sub>6</sub>)<sub>*n*</sub> chains lying on the substrate leading to [120] oriented ribbons,<sup>20</sup> and in the formation of dangling bonds and interfacial and GB defects resulting in poor PCE and higher *V*<sub>OC</sub> deficit. Therefore surface/interface modifications are needed to enhance PCEs.

### 3. Recombination processes and carrier transport in antimony selenide thin film solar cells

A typical thin-film Sb<sub>2</sub>Se<sub>3</sub> solar cell usually consists of a front contact, window layer, buffer layer, absorber layer, and back contact.<sup>1,3</sup> As a result, the overall performance of the solar cells is not only governed by the quality of the absorber layer but also the properties of other layers and interfaces. As described in Section 2.3, the defect states present in the interfaces between the absorber and transport layers are incredibly complicated and lead to carrier recombination and severe *V*<sub>OC</sub> deficit.<sup>1,3,55</sup> For solar cells, the main carrier recombination pathways include radiative recombination (photons), Auger recombination (electrons), and defect-assisted recombination. Compared to other thin-film PVs, it was recently reported that Sb<sub>2</sub>Se<sub>3</sub> devices exhibit weak Auger recombination such that it has a negligible influence on their performance.<sup>30,78</sup> These recombination pathways are identified to take place at different sites within the heterostructure, namely at the absorber surface, in the absorber bulk, at the absorber back contact, in the absorber space charge region (SCR), in the buffer layer, and finally in the window layer (Fig. 8).

When an active defect state energetically lies within the bandgap, it frequently captures or traps an approaching electron or hole, whereas when energy levels are shallow enough, the trapped carrier can escape through thermal energy. Under steady-state conditions, the detailed balance of carrier generation and recombination processes determines the performance of PV devices. Yet measuring the energy associated with each defect practically becomes difficult under open-circuit conditions. To understand the interface-induced recombination process and large *V*<sub>OC</sub> deficit following equation is used.<sup>3,37,59</sup>

$$V_{oc} = \frac{E_a}{q} - \frac{Ak_B T}{q} \ln \left( \frac{J_{00}}{J_{sc}} \right)$$

where *E*<sub>*a*</sub> is the activation energy for recombination, *A* is the ideality factor, *q* is the elemental charge, *T* is temperature, *k*<sub>B</sub> is the Boltzmann constant, *J*<sub>00</sub> is prefactor, and *J*<sub>SC</sub> is photocurrent density.

The carrier recombination mechanism in Sb<sub>2</sub>Se<sub>3</sub> solar cells can be identified by the *A* and the activation energy at 0 K.<sup>3,55</sup> Table 3 summarizes the reported *A* or activation energy of Sb<sub>2</sub>Se<sub>3</sub> solar cells in the literature. When all the parameters of Sb<sub>2</sub>Se<sub>3</sub> are well optimized, the *A* values of devices are found to be between 1 and 2, indicating that interface recombination is dominant, and SCR recombination may concomitantly participate in Sb<sub>2</sub>Se<sub>3</sub> solar cells when *A* is closer to 2.<sup>94,120</sup> In theory, if the bandgap is equal to or lower than the recombination activation energy, Shockley–Read–Hall (SRH) recombination in the SCR or neutral region of the absorber will dominate over interface recombination.<sup>3,59</sup> The activation energy of interface and SCR recombination in Sb<sub>2</sub>Se<sub>3</sub> solar cells is lower than the band gap, which is well in line with statistical results in Table 3



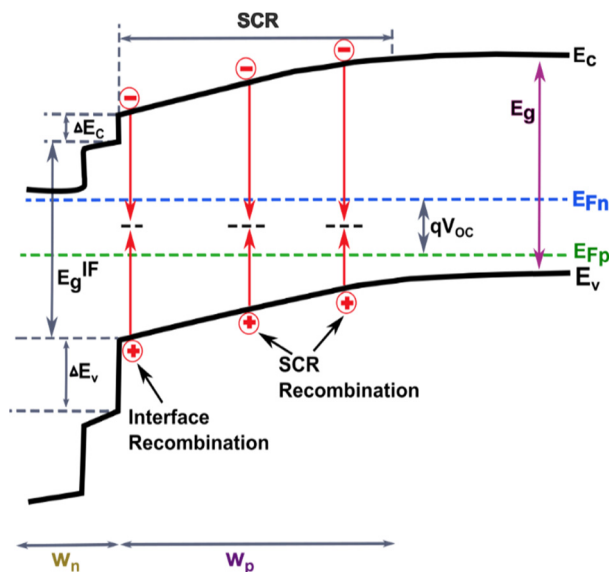


**Fig. 8** Schematic presentation of the possible recombination paths of heterostructure  $\text{Sb}_2\text{Se}_3$  solar cells under open-circuit conditions (where  $E_c$ ,  $E_v$ ,  $E_g$ ,  $E_g^{\text{IF}}$ ,  $w_n$ ,  $w_p$ , and  $E_{F_n}/E_{F_p}$  are denoted by the conduction band, valence band, bandgap, interface bandgap, width of the SCR in the buffer layer, width of the SCR in the absorber layer, and quasi-Fermi levels respectively).

and implies that the interface-induced recombination dominated over SCR recombination and contributes to the  $J_0$ .<sup>3,55,59</sup>

To gain further insight into the specific influence of each defect on the carrier dynamics and defect density states of the absorber, TRTA, time-resolved photoluminescence (TRPL), terahertz (THz) spectroscopy, and angular frequency-dependent capacitance were employed.<sup>7,39,72,79,80,123</sup> The activation energy of the dominant defects ( $V_{\text{sb}}$  and  $\text{Se}_{\text{sb}}$ ) of  $\text{Sb}_2\text{Se}_3$  is much larger than that of  $\text{Sb}_2\text{S}_3$  and kesterite materials,<sup>78</sup> which means that only 2.6% of the bulk defects of  $\text{Sb}_2\text{Se}_3$  contribute to the free carriers, leading to low free carrier density ( $7.7 \times 10^{13} \text{ cm}^{-3}$ ), limited bulk conductivity, and small quasi-Fermi level splitting under illumination. The  $N_{\text{T}}$  values of  $6.9 \times 10^{14} \text{ cm}^{-3}$  and  $1 \times 10^{15} \text{ cm}^{-3}$  were determined from space charge limited current measurement and first-principle calculation for  $\text{Sb}_2\text{Se}_3$  films at room temperature, respectively.<sup>78,121</sup> The same  $N_{\text{T}}$  of  $1 \times 10^{16} \text{ cm}^{-3}$  were detected by TAS.<sup>7</sup> From these studies,  $N_{\text{T}}$  in  $\text{Sb}_2\text{Se}_3$  was confirmed to be in the range of  $10^{14}$ – $10^{16} \text{ cm}^{-3}$ , and this value is 1–3 orders of magnitude greater than that of CdTe and CIGS

solar cells, implying significantly more disorder in  $\text{Sb}_2\text{Se}_3$  films.<sup>3</sup> Furthermore, conductivity measurements taken from temperature-dependent dark conductivity show that  $\text{Sb}_2\text{Se}_3$  films follow two different electrical conduction mechanisms.<sup>7,80</sup> Above 160 K, the electrical conductivity in films depends on the number of thermally activated carriers ionized from shallow defects over the inter grain potential barriers. Chen *et al.* showed intrinsic excitation dominates the carrier density from 250–420 K, and the activation energy (0.578 eV) is found to be half of the direct bandgap of  $\text{Sb}_2\text{Se}_3$ . On the other hand, at low temperatures (85–60 K) conductivity was reduced with the temperature as the conduction mechanism changed into Mott's variable range hopping between localized states in the bulk of the grains.<sup>7,80</sup>

Due to the presence of a large quantity of effective recombination centers at the interface originating from mismatched or imperfect energy level alignment to the energy barrier with the back contact, interdiffusion, and segregation of impurities, the rate of interface recombination is greater ( $\tau_1$ , shorter carrier lifetime) than that of SCR recombination ( $\tau_2$ , longer carrier lifetime). It has been found that a short lifetime of 0.1–1 ns (*i.e.*, interface/surface recombination)<sup>79,124</sup> and a long lifetime of 5–60 ns (*i.e.*, bulk defect recombination) (Table 4)<sup>7,72,79</sup> were commonly observed in  $\text{Sb}_2\text{Se}_3$ . These results revealed that the interface induced lifetime of  $\text{Sb}_2\text{Se}_3$  is far inferior to that of traditional absorbers, *i.e.*, CdTe ( $\sim 3.6 \mu\text{s}$ ), CIGS ( $\sim 250 \text{ ns}$ ), and CZTS ( $\sim 10 \text{ ns}$ )<sup>3,79</sup> due to a large capture cross-section, high density, and deep energy levels. In particular, Wang *et al.* revealed the surface recombination velocity of  $2 \times 10^3 \text{ cm s}^{-1}$ , which is much greater than that of CdTe ( $1.2 \text{ cm s}^{-1}$ ).<sup>79</sup>

Therefore, for reasonable carrier mobility and high electrical conductivity, carrier transport materials with proper band alignment, a minimum CBO and lower lattice mismatch are essential. To this end, wide-band gap buffer layers (CdS, ZnO,  $\text{TiO}_2$ , *etc.*) have been selected to improve the device performance, but the rises are often rather modest.<sup>18,19,38,92,113,117,125–128</sup> Furthermore, inorganic hole transport materials (HTM) such as  $\text{NiO}_2$ ,<sup>129</sup>  $\text{WO}_3$ ,<sup>130</sup>  $\text{MnS}_2$ ,<sup>131</sup> and organic HTMs like PCDTBT,<sup>9</sup> (PCPDTBT),<sup>52</sup> spiro-OMeTAD,<sup>32</sup> CZ-TA,<sup>45</sup> and  $\text{P}_3\text{HT}$ <sup>132</sup> have been introduced to enhance carrier extraction, passivate back contact defects and mitigate pinholes, but improvements in  $V_{\text{OC}}$  and PCEs are modest. Therefore, more suitable buffers and HTMs with high stability, low cost, low toxicity, matched energy level alignment, lower lattice mismatch, and simple preparation processes are needed to suppress the interfacial recombination and promote efficient carrier transport.

## 4. Extrinsic doping approaches

Absorber doping is a widely explored method to tune the thermoelectrical and photoelectrical properties of semiconductors by bandgap modulation,<sup>133,134</sup> improving film conductivity, increasing carrier concentration,<sup>135,136</sup> improving photoactivity,<sup>33,137</sup> increasing grain size,<sup>138</sup> regulating crystallization or morphology,<sup>103</sup> and passivating surface or grain boundaries.<sup>107</sup> Dopants can occupy the

**Table 3** Summary of ideality factor ( $A$ ) and activation energy ( $E_a$ ) of  $\text{Sb}_2\text{Se}_3$  solar cells

$A$	$E_a$ (eV)	$J_0$ ( $\text{mA cm}^{-2}$ )	$V_{\text{OC}}$ (V)	PCE (%)	Ref.
1.57	1.02	$1.00 \times 10^{-3}$	0.379	6.24	121
1.60	1.08	$2.80 \times 10^{-3}$	0.379	5.91	90
1.86	1.07	$4.30 \times 10^{-3}$	0.455	6.15	96
1.23		$2.75 \times 10^{-5}$	0.475	7.8	105
1.76		$1.56 \times 10^{-5}$	0.329	4.41	122
	1.06		0.391	5.93	19
	1.13		0.494	6.06	41



**Table 4** Summary of the shorter carrier lifetime ( $\tau_1$ ) and longer carrier lifetime ( $\tau_2$ ) of  $\text{Sb}_2\text{Se}_3$ 

Analysis method	Fabrication method	$\tau_1$ (ns)	$\tau_2$ (ns)	Ref.
TRTA	RTE	—	67	7
TRTA	VTD	1.339	—	39
TRTA	RTE	1.149	—	39
TRTA	Solution	0.01	5.25	32
TRPL	Solution	0.15	0.61	124
TRPL	Solution	0.13	0.32	124
TRPL	Solution	0.12	0.26	124
Calculation	VTD	—	21	90
Calculation	Sputtering	—	1–64	72
TA	Thermal evaporation	—	37.2	78
TA	Thermal evaporation	0.023	—	79
THz	Solution	0.03	—	124
THz	VTD	0.003–0.005	0.04	123
THz	Thermal evaporation	0.023	—	79

surface, GBs, or in the lattice by replacing host atoms and interstitial sites in the crystal structure, and these can either be isovalent or heterovalent. Cations with large diffusion coefficients and low diffusion barriers (*e.g.*,  $\text{Cu}^{2+}$ ,  $\text{Te}^{2+}$ ,  $\text{Pb}^{2+}$ , *etc.*) have been recognized as preferred dopants in  $\text{Sb}_2\text{Se}_3$  thin films for solar cells.<sup>32,105,107,139</sup> Despite the fact that both  $\text{Sb}_2\text{Se}_3$  and  $\text{Sb}_2\text{S}_3$  have similar Q1D structures, doping strategies used in  $\text{Sb}_2\text{S}_3$  have been reported to be similar compared to  $\text{Sb}_2\text{Se}_3$ .<sup>58,140</sup> Table 5 summarize advances that have been made in the doped  $\text{Sb}_2\text{Se}_3$  thin films solar cells and effect of dopants in  $\text{Sb}_2\text{Se}_3$  absorber for thin films solar cells are discussed below.

#### 4.1. Tin doping

Chen *et al.* reported a systematic study on Sn doping of  $\text{Sb}_2\text{Se}_3$  films using the conventional melt-quenching method in vacuum sealed silica tubes.<sup>99</sup> Pure  $\text{Sb}_2\text{Se}_3$  exhibits a low conductivity of  $2.71 \times 10^{-6} \text{ S cm}^{-1}$ , and the conductivity of Sn doped  $\text{Sb}_2\text{Se}_3$  was found to increase with increasing Sn content reaching higher conductivity of  $7.50 \times 10^{-2} \text{ cm}^{-3}$  at 0.1 at% of Sn. Incorporation of Sn was found to convert n-type pristine  $\text{Sb}_2\text{Se}_3$  films to p-type. Thus, suggesting that  $\text{Sn}^{4+}$  replaces the  $\text{Sb}^{3+}$  ions in the  $\text{Sb}_2\text{Se}_3$  matrix and as  $\text{Sn}^{4+}$  possesses two fewer

valence electrons, it acts as a hole donor at the doped site and therefore enhances the electrical conductivity, resulting in bulk charge-carrier density from  $1.44 \times 10^{11} \text{ cm}^{-3}$  ( $x = 0.00$ ) to  $1.94 \times 10^{16} \text{ cm}^{-3}$  ( $x = 0.10$ ). As a result of doping, dark current density increased from  $-16 \mu\text{A cm}^{-2}$  to  $-160 \mu\text{A cm}^{-2}$  at a bias voltage of  $-0.6 \text{ V}$ , and the photocurrent density increased from  $-18 \mu\text{A cm}^{-2}$  to  $-250 \mu\text{A cm}^{-2}$  at  $-0.6 \text{ V}$ . Interestingly, pristine  $\text{Sb}_2\text{Se}_3$  shows a direct band gap of 1.17 eV and Sn doping narrow band gap to 1.10 eV. The authors discussed narrow band gap absorber with specific doping levels is due to the Burstein–Moss shift and the renormalization effect.<sup>141,142</sup>

#### 4.2. Iron doping

Iron (Fe)-doped  $\text{Sb}_2\text{Se}_3$  films grown by electrodeposition have been studied by Costa *et al.*<sup>139</sup> The study showed that 5 at% Fe doping increases the carrier density from  $1.0 \times 10^{19} \text{ cm}^{-3}$  for undoped  $\text{Sb}_2\text{Se}_3$  to  $3.7 \times 10^{16} \text{ cm}^{-3}$  for doped  $\text{Sb}_2\text{Se}_3$ , which then exhibits p-type conductivity. However, doped  $\text{Sb}_2\text{Se}_3$  presented a similar photocurrent density ( $165.13 \mu\text{A cm}^{-2}$ ) to that of undoped films ( $166.34 \mu\text{A cm}^{-2}$ ) and further shows that Fe has a low influence on band gap and morphological properties of the films. It should be noted that this is true despite an extremely high doping concentration of the films. Furthermore, Li *et al.* also showed that Fe doped  $\text{Sb}_2\text{Se}_3$  has increased carrier mobility from  $9.0 \text{ cm}^2 \text{ V}^{-1} \text{ s}^{-1}$  to  $14.2 \text{ cm}^2 \text{ V}^{-1} \text{ s}^{-1}$  with negligible change in carrier concentration ( $4.9 \times 10^{13} \text{ cm}^{-3}$  in pristine  $\text{Sb}_2\text{Se}_3$  and  $3.4 \times 10^{13} \text{ cm}^{-3}$  in Fe doped- $\text{Sb}_2\text{Se}_3$ ).<sup>106</sup> However, in contrast to Costa *et al.*,<sup>139</sup> Kelvin probe force microscope and Hall measurements revealed that Fe doping changes poor p-type  $\text{Sb}_2\text{Se}_3$  thin-film to n-type. This significant discrepancy is likely to arise from the different defect types and their interactions in the two experimental environments.

#### 4.3. Lead doping

Pb-doping in  $\text{Sb}_2\text{Se}_3$  has been studied by Li *et al.* with an unspecified amount of dopants in the form of lead iodide ( $\text{PbI}_2$ ).<sup>143</sup> Their experiments showed that Pb doping enhances the hole concentration from  $1.6 \times 10^9$  to  $1.7 \times 10^{13} \text{ cm}^{-3}$  and  $V_{\text{OC}}$

**Table 5** Doping effect on the properties of  $\text{Sb}_2\text{Se}_3$  thin films

Dopant	Doping method	Doping concentration [at%]	Carrier concentration ( $\text{cm}^{-3}$ )	Doping type	Doping position	Ref.
Sn	Melt quenching	0.1	$1.94 \times 10^{16}$	p-type	In the lattice	99
Fe	Electro deposition	5	$1.0 \times 10^{19}$	p-type	In the lattice	139
Fe	Hydrazine solution process	0.1	$3.4 \times 10^{13}$	n-type	In the lattice	106
Pb	Magnetron sputtering	—	$1.7 \times 10^{13}$	p-type	In the lattice	143
I	Magnetron sputtering	0.1	—	n-type	In the lattice	44 and 68
Cl	Unintentional doping from starting materials	—	$10^{16}$ – $10^{17}$	n-type	—	108
Cu	$\text{CuCl}_2$ treatment	—	—	n-type	GBs	107
Te	Thermal evaporation	0.08	—	—	In the lattice	71
Te	Magnetron sputtering	0.03	—	n-type	In the spacing of $(\text{Sb}_4\text{Se}_6)_n$ ribbons	70
Te	Spin coating	2.2	—	n-type	GBs	32
Lanthanides	Co-reduction method at hydrothermal condition	0.04	—	—	In the lattice	148
S	Spin coating	5.34	—	—	—	32
Mg	Hydrazine solution process	0.1	$5.1 \times 10^{13}$	—	GBs or GIs	106
Na	Thermal evaporation	0.2	—	—	GBs or GIs	101



from 0.32 to 0.38 V, and the PCEs from 2.87% to 4.43%, indicating that  $\text{PbI}_2$  is an effective p-type dopant. Although the hole concentration increased, the mobility decreased from 18.7 to 1.3  $\text{cm}^{-2} \text{V}^{-1} \text{s}^{-1}$ , which may be due to deterioration of crystal quality, ionized impurity scattering, phonon scattering, and GB scattering originating from  $\text{PbI}_2$ . TA spectra show that  $\text{PbI}_2$  also passivates the GBs and suppresses interface recombination. Furthermore, this study showed that doping of lead as  $\text{Pb}^0$  metal showed no doping effect on  $\text{Sb}_2\text{Se}_3$ , which hints that  $\text{Sb}^{3+}$  is likely to be replaced by  $\text{Pb}^{2+}$  in the crystal structure.

#### 4.4. Halide doping

I doping into  $\text{Sb}_2\text{Se}_3$  by sputtering was carried out in two separate studies which suggest that I is an effective n-type dopant.<sup>44,68</sup> Ren *et al.* indicate that I successfully occupies the lattice sites of  $\text{Sb}_2\text{Se}_3$ , however, due to its larger size makes diffusion more difficult and significantly inhibits the growth of  $\text{Sb}_2\text{Se}_3$  grains.<sup>44</sup> In addition, Chen *et al.* were able to produce 0.1 at% I doped thin films with an increased photocurrent density of 770  $\mu\text{A cm}^{-2}$  compared to pristine at 0.7 V after post-heat treatment at 350 °C.<sup>68</sup>

Hobson *et al.* determined that unintentional Cl doping in purchased  $\text{Sb}_2\text{Se}_3$  material acts as a shallow dopant, significantly shifting the Fermi level position, and subsequent  $\text{Sb}_2\text{Se}_3$  films are n-type.<sup>108</sup> Here Cl doping occurs in both Se-rich and Se-poor conditions. However, in both chemical potential limits,  $\text{Cl}_{\text{Se}}$  appears to be the dominant defect due to its low formation energies ( $<0.5$  eV), Cl could easily substitute Se sites. Furthermore, the defects are compensated by  $V_{\text{Sb}}$  below the conduction band edge (0.3 eV), leading to significantly higher carrier concentrations in the range of  $10^{16}$ – $10^{17} \text{ cm}^{-3}$ . This demonstrated that in contrast to the standard p–n heterojunction architecture, a novel n–n isotype heterojunction  $\text{Sb}_2\text{Se}_3$  solar cell formed at  $\text{TiO}_2/\text{Sb}_2\text{Se}_3$  interface. Further DFT calculations illustrated that with the proper band alignment and higher carrier concentration, the Cl doped  $\text{Sb}_2\text{Se}_3$  solar cells can achieve a PCE of 7.3%.<sup>108</sup> However, considering the deep-level compensating defects caused by Cl, anion doping is still needed in future research.

#### 4.5. Copper doping

The PCEs of  $\text{Sb}_2\text{Se}_3$  are mostly hindered by deep level defect recombination at vacancy defects ( $V_{\text{Se}}$ ) and substitutional defects ( $\text{Se}_{\text{Sb}}$  or  $\text{Sb}_{\text{Se}}$ ). The spatial separation of carriers at deep defect centers creates an electric field between GBs and grain interiors (GIs). As discussed earlier,  $\text{Sb}_2\text{Se}_3$  films are often weakly p-type, and the introduction of dopants was found to convert GBs into n-type. This will then lead to the Fermi level difference between GBs and GIs, which induce an electric field from GBs to GIs creating electrons to pass through GBs and holes through GIs. The GB inversion, therefore, restrains the electron–hole recombination. For this process, effective n-type doping has been carried out using metal cation interstitial doping (such as  $\text{Cu}^{2+}$ ) or substitutional doping by halogens (such as I).<sup>44,107</sup> The introduction of  $\text{CuCl}_2$  in aqueous ammonia ( $\text{NH}_3$ ) at low temperatures induces the diffusion of  $\text{Cu}^{2+}$  ions into  $\text{Sb}_2\text{Se}_3$  films along the GBs, as has been utilized

extensively for CdTe devices.<sup>144</sup> Chen *et al.* showed that a built-in electric field was established under the addition of  $\text{Cu}^{2+}$  between p-type GIs and n-type GBs, forming an interstitial defect ( $\text{Cu}_i$ ).<sup>107</sup>  $\text{CuCl}_2$  treatment reduces the surface potential of GBs compared to the control sample causing uplift of the Fermi level very close to the conduction band of  $\text{Sb}_2\text{Se}_3$ , confirming the n-type inversion at GBs. Consequently, spatial separation of photogenerated carriers suppresses nonradiative recombination at GIs, enhances carrier collection, and improves the  $V_{\text{OC}}$  and  $J_{\text{SC}}$  of the device. DFT simulations show the origin of the n-type inversion after  $\text{CuCl}_2$  treatment in  $\text{Sb}_2\text{Se}_3$  to be substitutional  $\text{Cu}_{\text{Sb}}$  (an acceptor, increasing p-type conductivity) and interstitial  $\text{Cu}_i$  (a donor, increasing n-type conductivity). Under Se-rich conditions, the formation energies for the two doping sites are both high ( $>1$  eV), whereas in Se-poor conditions,  $\text{Cu}_i$  has a much lower formation energy (0.75 eV) than  $\text{Cu}_{\text{Sb}}$  (1.46 eV), indicating that  $\text{Cu}_i$  is easier to form than  $\text{Cu}_{\text{Sb}}$ .<sup>107</sup>

#### 4.6. Tellurium doping

As mentioned previously, under Se-rich conditions,  $\text{Se}_{\text{Sb}}$  and  $V_{\text{Sb}}$  are dominant in  $\text{Sb}_2\text{Se}_3$  films and directly affect the device performance.<sup>39</sup> Ma *et al.* demonstrated an effective strategy to remove these acceptor defects in Se-rich  $\text{Sb}_2\text{Se}_3$  films by introducing 2.2 at% Te.<sup>32</sup> Unlike other metal elements, Te can regulate the atomic ratio of Se/Sb in  $\text{Sb}_2\text{Se}_3$  films by competitively reacting with Se to form  $\text{Sb}_2\text{Te}_3$ -doped  $\text{Sb}_2\text{Se}_3$  instead of an  $\text{Sb}_2(\text{Se},\text{Te})_3$  alloy. DLTS analysis showed that pristine  $\text{Sb}_2\text{Se}_3$  solar cells displayed three deep traps corresponding to two-hole traps  $H_1$  ( $E = 0.48$  eV,  $N_T = 6.10 \times 10^{14} \text{ cm}^{-3}$ ),  $H_2$  ( $E = 0.71$  eV,  $N_T = 1.00 \times 10^{15} \text{ cm}^{-3}$ ) and one electron trap  $E_1$  ( $E = 0.63$  eV,  $N_T = 6.49 \times 10^{14} \text{ cm}^{-3}$ ) whereas Te doped  $\text{Sb}_2\text{Se}_3$  films displayed one hole trap  $H_1$  ( $E = 0.48$  eV,  $N_T = 5.34 \times 10^{13} \text{ cm}^{-3}$ ) and one electron trap  $E_1$  ( $E = 0.64$  eV,  $N_T = 3.32 \times 10^{14} \text{ cm}^{-3}$ ). Typically, the hole traps (acceptor defects) with defect energy levels  $H_1$  and  $H_2$  are indexed to  $V_{\text{Sb}}$  and  $\text{Se}_{\text{Sb}}$ , respectively, and electron traps  $E_1$  (donor defects) correspond to  $\text{Sb}_{\text{Se}}$ . The pristine  $\text{Sb}_2\text{Se}_3$  device delivered a PCE of 3.3%, with  $J_{\text{SC}}$  of 21.6  $\text{mA cm}^{-2}$ ,  $V_{\text{OC}}$  of 312 mV, and FF of 48.2%. Deep level acceptor defects ( $\text{Se}_{\text{Sb}}$ ) were found to be completely suppressed by 2.21 at% Te-doped  $\text{Sb}_2\text{Se}_3$  films, greatly reducing the charge recombination and thus rendering a longer carrier lifetime giving rise to pronounced enhancement in PCEs to 5.4% ( $J_{\text{SC}}$  29.0  $\text{mA cm}^{-2}$ ,  $V_{\text{OC}}$  360 mV, and FF 51.5%). Although the work claims to have completely mitigated deep defects in  $\text{Sb}_2\text{Se}_3$ , the improvement of  $V_{\text{OC}}$  is not that significant. The film resistivity for the pristine device is recorded as 2196  $\Omega \text{ cm}^2$ , while Te-doped device increases to 7843  $\Omega \text{ cm}^2$ . The remarkable increase in recombination resistance suggests the 2.21 at% Te doping  $\text{Sb}_2\text{Se}_3$  based device prevents charge recombination more efficiently than the pristine  $\text{Sb}_2\text{Se}_3$  based device. This reduced recombination probability contributes to the enhancement in  $V_{\text{OC}}$  and FF of the device. Another study of Te doping in  $\text{Sb}_2\text{Se}_3$  solar cells was reported by employing the thermal evaporation technique.<sup>71</sup> As compared to the control device without doping, the device with an optimal doping concentration of 0.08 at% showed an unusual increase in optical band



gap from 1.46 to 1.65 eV, which was then ascribed to the crystallization of multiple Sb–Se phases with higher bond energies. However, the conductivity of doped films was reduced to  $1.22 \times 10^{-7} \Omega^{-1} \text{cm}^{-1}$  compared to undoped  $\text{Sb}_2\text{Se}_3$   $2.55 \times 10^{-7} \Omega^{-1} \text{cm}^{-1}$ . The authors show the decrease in the conductivity may be due to the reduction in thermal activation energy, which may be due to defects at GBs, voids, and surface imperfections. But a detailed analysis of defects associated with each GB and surface corresponding to the  $V_{\text{OC}}$  and PCE is not provided. However, an Urbach energy of 0.12 eV recorded for pure  $\text{Sb}_2\text{Se}_3$  films and 0.16 eV for 0.08 at% Te doped films, is lower compared to other reported values.<sup>55</sup> The Raman spectra prove that the Te inclusion tunned the Se/Sb ratio of  $\text{Sb}_2\text{Se}_3$  and formed intermixed alloys such as  $\text{Sb}_2\text{Te}_3$ -doped  $\text{Sb}_2\text{Se}_3$  instead of the  $\text{Sb}_2(\text{Se},\text{Te})_3$  alloy. In addition, the Te doping was found to mitigate the surface oxidation of  $\text{Sb}_2\text{Se}_3$  and reduce the optical absorption and absorption coefficient (from  $0.89 \times 10^4 \text{cm}^{-1}$  to  $0.75 \times 10^4 \text{cm}^{-1}$ ) compared to the pristine  $\text{Sb}_2\text{Se}_3$  film, which in agreement with the previous report.<sup>145</sup>

Furthermore, Ren *et al.* investigated the Te doping in  $\text{Sb}_2\text{Se}_3$  by magnetron sputtering.<sup>70</sup> This shows that Te atoms were accommodated into the spacing of  $[\text{Sb}_4\text{Se}_6]_n$  ribbons rather than in the lattice and formed n-type  $\text{Sb}_2\text{Se}_3$ . It was found that post-deposition annealing at 325 °C had a crucial influence on the photocurrent density of films, and a current density of  $1.91 \text{mA cm}^{-2}$  was recorded for annealed films. Moreover, due to the change in atomic arrangement from disorder to ordered structure, the band gap of as-deposited films (1.65 eV) decreased to around 1.27 eV after annealing. Similar to Sn doping, an increase in the band gap with respect to pristine  $\text{Sb}_2\text{Se}_3$  thin films (1.15 eV) was attributed to a combination of the Burstein–Moss shift and the renormalization effect, existing in the narrow band gap semiconductor with a certain doping level.<sup>141,142</sup>

#### 4.7. Lanthanide doping

Alemi *et al.* have incorporated large electropositive ions, such as the lanthanides (holmium ( $\text{Ho}^{3+}$ ), neodymium ( $\text{Nd}^{3+}$ ), lutetium ( $\text{Lu}^{3+}$ ), samarium ( $\text{Sm}^{3+}$ ), gadolinium ( $\text{Gd}^{3+}$ ), erbium ( $\text{Er}^{3+}$ ), and ytterbium ( $\text{Yb}^{3+}$ )) into the  $\text{Sb}_2\text{Se}_3$  lattice by the hydrothermal co-reduction method.<sup>102–104,146,147</sup> However, these studies show that the incorporation of  $\text{Gd}^{3+}$  and  $\text{Sm}^{3+}$  into  $\text{Sb}^{3+}$  sites form a  $\text{Ln}_x\text{Sb}_{2-x}\text{Se}_3$  structure. This is isostructural with  $\text{Sb}_2\text{Se}_3$  and does therefore not change the morphology of  $\text{Sb}_2\text{Se}_3$ .<sup>102</sup> According to differential scanning calorimetry, the electrical conductance of lanthanide-doped materials was enhanced compared to undoped  $\text{Sb}_2\text{Se}_3$  at room temperature (*i.e.*, pure  $\text{Sb}_2\text{Se}_3$ ;  $0.2 \Omega \text{m}$  and  $\text{Sb}_{1.96}\text{Gd}_{0.04}\text{Se}_3$ ;  $6 \times 10^{-2} \Omega \text{m}$ ).<sup>102,147</sup> However, substitution of  $\text{Sb}^{3+}$  with  $\text{Yb}^{3+}$  and  $\text{Er}^{3+}$  leads to morphology changes from nanorods to nanoflowers,<sup>103</sup> while  $\text{Sb}_2\text{Se}_3$  films co-doped with  $\text{Lu}^{3+}/\text{Yb}^{3+}$  ( $\text{Lu}_{0.04}\text{Yb}_{0.04}\text{Sb}_{1.92}\text{Se}_3$ ) and  $\text{Lu}^{3+}/\text{Er}^{3+}$  ( $\text{Lu}_{0.04}\text{Er}_{0.04}\text{Sb}_{1.92}\text{Se}_3$ ) produce nanorods and nanoparticles, respectively. Besides, the electrical resistivity of co-doped  $\text{Sb}_2\text{Se}_3$  ( $0.009 \Omega \text{m}$  for  $\text{Lu}^{3+}/\text{Yb}^{3+}$ ,  $0.032 \Omega \text{m}$  for  $\text{Lu}^{3+}/\text{Er}^{3+}$ ) is lower than that of the pure  $\text{Sb}_2\text{Se}_3$  ( $0.200 \Omega \text{m}$ ) and decreased linearly with temperature.<sup>148</sup> Therefore, lanthanide doping has been shown to promote the

electrical conductivity of  $\text{Sb}_2\text{Se}_3$  as well as thermoelectrical conductivity.

In addition to the dopants discussed above, alkaline metals such as sodium (Na) and magnesium (Mg), or chalcogenide atoms like S have been used to doped  $\text{Sb}_2\text{Se}_3$  films (Table 5).<sup>101,106,139</sup> However, segregation of dopants such as Na and Mg into GBs or GIs makes them largely inactive which makes film properties and device performance are independent from the presence of these dopants.<sup>76,101</sup> The concentration of dopants inclusive in  $\text{Sb}_2\text{Se}_3$  thin films is questionable. Therefore, at higher concentrations of dopants, excess metal dopants were found to be present compared to Se and Sb, which often forms solid solutions or discreet secondary phases instead of doping.<sup>149</sup> Therefore, a complete understanding of the absorber-dopant correlation is essential for the future development of PVs.

## 5. Suppression of defects

Defect modulation at the surfaces and interfaces in  $\text{Sb}_2\text{Se}_3$  thin films is a key issue in defect engineering and plays a vital role in modifying the functional properties of the material. The core aspect of defect engineering lies in modulating the concentration and spatial configuration of defects. This mainly depends on the Sb and Se chemical potential during film deposition, substrate modification, post-processing treatment, and interfacial modification. Although great advances have been achieved to mitigate defects, atomic-level understanding of the defect passivation mechanism for different passivators has not been fully explored (*i.e.*, the interaction between GBs/surface defects and passivation techniques). Therefore, it is essential to understand the underlying working mechanism of passivators, which could guide researchers towards an effective passivation strategy for  $\text{Sb}_2\text{Se}_3$  and other absorber materials. This section reviews recently reported techniques to suppress defects associated with absorbers that are used to overcome  $V_{\text{OC}}$  bottleneck and defect-assisted recombination.

### 5.1. Suppressing defects through post-annealing treatment

Post-deposition annealing treatment is one of the most efficient methods to improve film quality *via* increasing the crystallinity, tuning the crystal orientation, increasing grain size, decreasing porosity, and reducing defect concentration.<sup>139,150</sup> Post-annealing treatment on  $\text{Sb}_2\text{Se}_3$  films has been carried out in different annealing conditions, *i.e.*, air, vacuum, argon (Ar), nitrogen ( $\text{N}_2$ ), and Se vapor.<sup>63,94,151</sup> Leng *et al.* demonstrated that post-annealing of thermally evaporated  $\text{Sb}_2\text{Se}_3$  films in a Se atmosphere compensates for Se loss during thermal evaporation and increases the doping density from  $1.3 \times 10^{16}$ – $2.4 \times 10^{16} \text{cm}^{-3}$  to  $1.7 \times 10^{16}$ – $2.6 \times 10^{16} \text{cm}^{-3}$ . This attenuated the  $V_{\text{se}}$  associated recombination loss and resulted in improved device efficiency from 1.9% to 3.7%.<sup>63</sup> Photoelectrochemical analysis (photocurrent–potential and photovoltage tests) confirmed p-type conductivity for potentiostatic electrodeposited  $\text{Sb}_2\text{Se}_3$  films.<sup>151</sup> As deposited films showed an optical absorption coefficient of  $1.95 \times 10^5 \text{cm}^{-1}$ , and when these films were annealed at 300 °C in Ar atmosphere,





the absorption coefficient decreased to  $1.61 \times 10^5 \text{ cm}^{-1}$ . Authors claimed that higher absorption coefficient of the as-deposited films exhibited due to the poorer crystallinity and higher defect density which then may act as light absorption centers, whereas post-annealing enhances the crystallinity. Photoelectrochemical tests revealed excellent photoelectrochemical activity in annealed samples which is evident in the reduction of defect densities. Furthermore, C-F measurement of post-annealed VTD films at  $200 \text{ }^\circ\text{C}$  in vacuum conditions showed three defect levels at 352, 440, and 606 eV in the bandgap with  $N_T$  of  $1.9 \times 10^{14}$ ,  $6.7 \times 10^{14}$ , and  $3.3 \times 10^{15} \text{ cm}^{-3}$  respectively. Whereas unannealed films showed three defect levels but at higher thermal activation energy with higher  $N_T$ . This shows that  $N_T$  of the post-annealed sample was lower compared to pristine films, and therefore the net carrier concentration increased from  $1.13 \times 10^{17} \text{ cm}^{-3}$  to  $1.30 \times 10^{17} \text{ cm}^{-3}$ , raising the efficiency from 4.89% to 5.72%.<sup>94</sup> However, heat treatment post deposition induced more Cd and S inter-diffusion across CdS/Sb<sub>2</sub>Se<sub>3</sub>, demonstrating that there can be negative consequences to post-deposition annealing.<sup>34</sup> Post-annealing at  $300 \text{ }^\circ\text{C}$  under an inert environment caused delamination of the antimony oxide (Sb<sub>2</sub>O<sub>3</sub>) from the Sb<sub>2</sub>Se<sub>3</sub>. However, annealing of Sb<sub>2</sub>Se<sub>3</sub> in the presence of O<sub>2</sub> was found to passivate V<sub>se</sub> defects leading to lower defect densities and reduced defect energy levels. Five characteristic activation energies at 0.326, 0.446, 0.381, 0.536, and 0.489 eV were obtained for unannealed samples, whereas three activation energy levels were obtained for annealed devices at 0.344, 0.509, and 0.475 eV.<sup>119</sup> Furthermore, annealing at higher temperatures such as 400 and 500 °C caused crystallographic texturing of films in the [120] direction, which diminishes its PV properties.<sup>139,150</sup> Further, Ma *et al.* prepared Sb<sub>2</sub>Se<sub>3</sub> thin films by co-sputtering of Sb<sub>2</sub>Se<sub>3</sub> and Se targets with a substrate temperature of 350 °C without a subsequent annealing process, exhibited better crystallinities and a preferred orientation along the [221] direction.<sup>152</sup>

## 5.2. Suppressing defects through post-selenization treatment

Based on the above results, it has been found that Sb<sub>2</sub>Se<sub>3</sub> films possess donor defects that are difficult to manipulate due to a Sb or Se elemental imbalance. Thermally fabricated Sb<sub>2</sub>Se<sub>3</sub> films were mostly Se poor, in which deep level defects such as Sb<sub>se</sub> and V<sub>se</sub> dominantly act as carrier traps. Therefore, post-selenization or *in situ* selenium compensation processes are critical to produce films with an optimal elemental ratio (Sb/Se = 0.666) to restrain detrimental intrinsic Se defects related to recombination.<sup>30,78</sup> Thus, adjusting the element ratios and passivating the volatilization of chemical components are crucial methods to minimize recombination centers of carriers (electron traps/hole traps) at buffer/Sb<sub>2</sub>Se<sub>3</sub> and HTL/Sb<sub>2</sub>Se<sub>3</sub> interfaces, enhance photoresponse, and increase photocurrent.<sup>32,78</sup> Liu *et al.* further revealed an additional selenization step provides excess Se to compensate for the Sb<sub>se</sub> and V<sub>se</sub> defects that originated from thermal evaporation.<sup>78</sup> Two defects were depicted for the as-produced Se-poor Sb<sub>2</sub>Se<sub>3</sub> films at 308 and 518 meV and for Se compensated films (Se-rich) at 107 and 503 meV. It can be shown that defects present in pristine films

can be deep donor defects, either Sb<sub>se</sub> or V<sub>se</sub> or both in high concentrations. However, under Se-rich conditions, the defects activation energy of Sb<sub>se</sub> or V<sub>se</sub> are lowered, and Se<sub>sb</sub> acceptor defects are introduced at 100 meV depth below the CBM.<sup>30</sup> The beneficial effects of Se compensation enhanced the photocarrier lifetime up to 102 ns, which is 2.5 times longer than the pristine device. Enhanced photocarrier lifetime was attributed to lower charge recombination loss and improved quality of the CdS/Sb<sub>2</sub>Se<sub>3</sub> heterojunction with lower interfacial and bulk defects leading to a PCE of 5.76% ( $J_{sc}$  of  $26.3 \text{ mA cm}^{-2}$ ,  $V_{oc}$  of 0.38 V, and FF of 57%). In addition, Tang *et al.* proposed a post-selenization treatment for magnetron sputtered Sb<sub>2</sub>Se<sub>3</sub>.<sup>41</sup> This study revealed deposition temperatures can vary the Sb/Se ratio of Sb<sub>2</sub>Se<sub>3</sub> films, that Se-poor films with an Sb/Se ratio of 0.688 were obtained at a selenization temperature of 420 °C and had a minimum defect density of  $9.29 \times 10^{15} \text{ cm}^{-2}$  with an activation energy of 456 meV. Moreover, C-V profiling and DLCP suggested a lower interfacial defect density of  $1.88 \times 10^{11} \text{ cm}^{-2}$  and a reduction of recombination at the CdS/Sb<sub>2</sub>Se<sub>3</sub> interfaces, increasing the PCE to 6.06% with an outstanding  $V_{oc}$  of 0.494 V. Moreover, Liang *et al.* reported a PCE of 6.84% with an impressive  $V_{oc}$  of 0.504 V for Sb<sub>2</sub>Se<sub>3</sub> solar cells prepared by selenization of the sputtered Sb precursor thin films.<sup>34</sup> Although a higher  $V_{oc}$  was recorded, post-selenization heat treatment induced an insufficient selenization or crystallization of Sb<sub>2</sub>Se<sub>3</sub> films leaving the films Se deficient (Sb/Se ratio of 0.67). Moreover, severe stoichiometric deviations to Se-poor films (Sb/Se = 0.69) are prone to produce defects with high  $N_T$  of  $1.32 \times 10^{16} \text{ cm}^{-3}$  and  $1.38 \times 10^{16} \text{ cm}^{-3}$  and activation energy of 310 meV and 407 meV, respectively. Besides, Li *et al.* revealed that electron beam evaporated Sb followed by selenization at temperatures above 360 °C gradually changes the grains from round shape to rod-like shape introducing some craters and cracks in the films.<sup>153</sup> Sb<sub>2</sub>Se<sub>3</sub> films fabricated at 360 °C showed an average grain size of 450 nm, an optical bandgap of 1.24 eV, carrier concentration of  $4.99 \times 10^{12} \text{ cm}^{-3}$ , and a carrier mobility of  $6.88 \text{ cm}^2 \text{ V}^{-1} \text{ s}^{-1}$ , which are comparable with reported values of Liu *et al.*<sup>67</sup> Selenization of Sb<sub>2</sub>Se<sub>3</sub> films deposited on Mo-coated glass substrates by CSS at 425 °C shows to increase in the grain size (0.87 to 2.68 μm), crystallinity, and improved the orientation of the films, which results in a reduced V<sub>se</sub> related recombination loss, particularly at Sb<sub>2</sub>Se<sub>3</sub> ribbon edges and GBs.<sup>64</sup> With all these benefits of proper selenization, a significant carrier density of  $7.21 \times 10^{16} \text{ cm}^{-3}$  and device performance improvement of 1.85% to 6.43% is achieved. Besides, the selenization treatment also facilitates the formation of a thin MoSe<sub>2</sub> layer at the Sb<sub>2</sub>Se<sub>3</sub>/Mo interface, which helps to improve the back-interface quality and eliminate the Schottky barrier, and reduces the recombination at the back interface improving PCE from 3.66 to 7.07%.<sup>154</sup> Yao *et al.* presented selenized annealing in a hydrogen sulfide (H<sub>2</sub>S) gas atmosphere, which largely compensates for deficiencies of Se and removes the Sb<sub>2</sub>O<sub>3</sub> layer on the film surface.<sup>155</sup> H<sub>2</sub>S treatment significantly decreased the charge-recombination in bulk films and enhanced the carrier lifetime. As a result of improved crystallinity and compensation of Se, higher carrier mobility of  $45.57 \text{ cm}^2 \text{ V}^{-1} \text{ s}^{-1}$  was obtained.



The DFT and experimental studies by Huang *et al.* and Fuentes *et al.* showed that a defect engineering strategy with post deposition selenization processing and Se-rich conditions is invalid for  $\text{Sb}_2\text{Se}_3$ .<sup>84,156</sup> Huang *et al.* showed that formation energy and density of the anion vacancy  $V_{\text{Se}}$  depend not only on the Se chemical potential but also on the Fermi level. As the Fermi level is determined by the density of all ionized donor and acceptor defects, the formation energy and density of all ionized defects are influenced by each other. Therefore, under Se-rich conditions  $\text{Sb}_2\text{Se}_3$  formation energy of  $V_{\text{Se}_2}^{2+}$  and  $V_{\text{Se}_3}^{2+}$  decreases, and thus their defect densities increase, leading to more detrimental carrier traps. Fuentes *et al.* has experimentally confirmed that a very high Se content deteriorates the PCE due to degraded  $J_{\text{SC}}$  and FF.<sup>156</sup> Similar abnormal behavior may be common in  $\text{Sb}_2\text{S}_3$  and  $\text{Sb}_2(\text{S},\text{Se})_3$ .

### 5.3. Suppressing defects through surface treatments

External additives have been introduced to the surface of the  $\text{Sb}_2\text{Se}_3$  films in order to reduce defect states.<sup>107,109,157,158</sup> At lower evaporation temperatures, due to the high partial pressure of Se, more Se-rich vapor compositions are expected to form, making elemental Se agglomerate on top of  $\text{Sb}_2\text{Se}_3$  films. Chen *et al.* showed ammonium sulfide  $(\text{NH}_4)_2\text{S}$  etching can be an effective strategy to remove  $\text{Sb}_2\text{O}_3$  and elemental Se from the  $\text{Sb}_2\text{Se}_3$  back surface<sup>107,109</sup> although a greater understanding of how these treatments function is required.<sup>159</sup>  $(\text{NH}_4)_2\text{S}$  post-treatment might passivate the surface of  $\text{Sb}_2\text{Se}_3$  film *via* removing  $\text{Sb}_2\text{O}_3$  and impure phases of Se, possibly through the formation of soluble  $\text{Se}_8$  ring species at the back contact. This would therefore improve the back contact quality and decrease the contact resistance, attenuating recombination losses.<sup>107,109</sup>  $\text{NH}_3$  etching tailored the bandgap alignment of the  $\text{CdS}/\text{Sb}_2\text{Se}_3$  heterojunction from a “cliff-like” to a “spike-like” structure. Interestingly  $\text{NH}_3$  removes O-containing impurities derived from  $\text{CdS}$  thin films, *e.g.*,  $\text{CdO}$ ,  $\text{Cd}(\text{OH})_2$ , or surface-adsorbed OH groups located at the GBs, which reduced carrier recombination and enhanced crystal orientation leading to an improved PCE of 7.48%.<sup>158</sup> Carbon disulfide ( $\text{CS}_2$ ) was found to remove excess amorphous Se residue which often condenses onto the surface of RTE-produced  $\text{Sb}_2\text{Se}_3$  absorber layer during the cooling stage.  $\text{CS}_2$  thus eliminates the contact barrier and improves the FF of films significantly.<sup>19</sup> In contrast to previous work, Shiel *et al.* showed in close space sublimation (CCS) fabricated  $\text{Sb}_2\text{Se}_3$  films,  $(\text{NH}_4)_2\text{S}$  etch increases the proportion of free Se, making more Se-rich films and there is no or little effect on the amount of free Se at the back contact surface by  $\text{CS}_2$  etch.<sup>159</sup>

Furthermore, the use of potassium hydroxide (KOH) solution as the etchant not only increases the efficiency of  $\text{Sb}_2\text{Se}_3$  solar cells but also increases the doping density from  $2.82 \times 10^{16}$  to  $3.37 \times 10^{16} \text{ cm}^{-3}$  and improves the back contact. At an appropriate concentration of KOH, crystallinity, optical properties,  $V_{\text{OC}}$  (0.335 to 0.407 V), FF (51 to 57.4%), and shunt resistance of the device significantly improved, promoting the efficiency of the carrier transport while suppressing recombination.<sup>157</sup> In addition, a thin layer of  $\text{Sb}_2\text{O}_3$  formed

during the KOH etching process, and the introduction of this layer was found to passivate interface defects and increase the ohmic contact of the device. This shows that  $\text{O}_2$  is an intriguing contaminant in  $\text{Sb}_2\text{Se}_3$  solar cells. Learning from  $\text{CdTe}$  solar cells,<sup>160</sup> the controlled addition of  $\text{O}_2$  during the thermal evaporation of  $\text{Sb}_2\text{Se}_3$  films significantly yields an efficiency improvement to 4.8%. In addition, proper  $\text{O}_2$  partial pressure could substantially enhance the  $\text{CdS}/\text{Sb}_2\text{Se}_3$  heterojunction quality through effective interfacial defect passivation. Thus,  $\text{O}_2$  coupling with  $\text{Sb}_2\text{Se}_3$  is attributed to reducing defect states at the interface but also harming device performance by the formation of  $\text{Sb}_2\text{O}_3$  on the surface of  $\text{Sb}_2\text{Se}_3$ . The presence of  $\text{Sb}_2\text{O}_3$  on films will act as the charge trap, leading to back surface recombination losses and a decrease in device performance.<sup>33,161</sup> Therefore, the controlled addition of  $\text{O}_2$  in device fabrication may be necessary to increase the p-type doping, increase the built-in potential to reduce series resistance, improve minority carrier lifetime, suppress recombination and elevate solar cell efficiency.<sup>33</sup>  $\text{Sb}_2\text{Se}_3$  films were mostly annealed in an inert gas medium to prevent rapid oxidation by air. However, even during the annealing or when cooling the evaporation chamber of thermally deposited (VTD/RTE/CCS)  $\text{Sb}_2\text{Se}_3$  under the typical medium vacuum conditions (1–3 Pa),  $\text{O}_2$  residue in the chamber could react with  $\text{Sb}_2\text{Se}_3$  to form a thin layer of oxide.<sup>150,161,162</sup> Kamruzzaman *et al.* shown standard molar formation enthalpy and Gibbs free energy of Sb with  $\text{O}_2$  larger than that of the Sb and Se reaction. Here due to low O chemical potential a non-stoichiometric Sb–O layer is formed, highlighting the strong Sb–O chemical affinity.<sup>150</sup> Wang *et al.* showed hydrochloric acid (HCl) treatment resulted in the reduced Sb–O content evident in a substantial reduction of the Sb–O/ $\text{Sb}_2\text{Se}_3$  ratio. To date, the influence of oxide contamination on the electrical properties of bulk  $\text{Sb}_2\text{Se}_3$  or at the p–n junction is not well understood, but removing this layer from  $\text{Sb}_2\text{Se}_3$  was found to yield a 13–14% relative improvement in solar cell performance.<sup>162</sup> Moreover,  $\text{H}^+$  and  $\text{Cl}^-$  ions can diffuse into GBs and alter their electrical nature.<sup>107</sup> However, interdiffusion of  $\text{Cl}^-$  to the bulk of  $\text{Sb}_2\text{Se}_3$  was found to be difficult due to the short etching period, but this could be expedited during annealing treatments. Although HCl removed the back contact Sb–O and altered the electrical properties of GBs, it can also dissolve the  $\text{Sb}_2\text{Se}_3$  absorber resulting in unfavorable circumstances. Therefore, a deeper understanding of the effect of HCl etching treatments on GBs is required.

## 6. Conclusions and outlook

This article comprehensively reviews the defect chemistry of  $\text{Sb}_2\text{Se}_3$  thin-film solar cells with a focus on the origin (*i.e.*, surface, GBs, and interface), defect types (*i.e.*, intrinsic and extrinsic), defect formation energy under different environments (*i.e.*, Se-rich and Se-poor), defect density, distribution, and on their role in PV performance. Innovative strategies in defect engineering are also discussed, including dopant engineering, post-annealing treatment, Se environment, surface-treatment,



and interlayer passivation methods to suppress surface and interface defects. It is now generally accepted that a reduction of non-radiative recombination losses, including defect-assisted recombination and interface-induced recombination in  $\text{Sb}_2\text{Se}_3$  films is an effective strategy to further improve the  $V_{\text{OC}}$  of  $\text{Sb}_2\text{Se}_3$  thin-film solar cells. Carefully managed passivation methods have the capacity to inhibit defect-assisted carrier recombination by eliminating deep level defect states resulting in enhanced film properties, such as increased grain size, bandgap modulation, energy level passivation, and increased carrier concentration. Although the strategies discussed substantially minimize negative defects and associated recombination losses, there has not been a subsequent significant increase in the  $V_{\text{OC}}$ , and this is due to a lack of clear understanding of defects and their evolution in  $\text{Sb}_2\text{Se}_3$  during device operation.

To date, various methods have been employed to remove or reduce the deep defects in  $\text{Sb}_2\text{Se}_3$  solar cells. Despite the progress of passivation techniques, many important questions remain unanswered and a deeper understanding of the influence of preparation methods on defect formation, interface defect properties, recombination mechanisms, and carrier transport dynamics of  $\text{Sb}_2\text{Se}_3$  solar cells is needed. Recently, extrinsic dopants have been used to modify the optoelectronic properties and device performance of  $\text{Sb}_2\text{Se}_3$  solar cells. Although doping is an effective strategy for modulating defects, controlling doping levels and carrier concentrations is difficult in  $\text{Sb}_2\text{Se}_3$  films.

Band alignment optimization and interface defect passivation to control the interface recombination is achieved by various buffer materials (e.g., CdS,  $\text{TiO}_2$ , ZnO) and heterojunction bilayers (e.g., CdS/ $\text{TiO}_2$ , CdS/ZnO). Whilst this has yielded efficiency improvements, it is important to consider that much of what has driven researchers to consider  $\text{Sb}_2\text{Se}_3$  as a strong candidate for a future PV absorber material is the low toxicity and earth-abundant nature and that the introduction of toxic and scarce elements such as Cd, Pb, and Te preclude these benefits and will therefore deviate from the sustainable development of  $\text{Sb}_2\text{Se}_3$  solar cells. Therefore, research must focus on developing  $\text{Sb}_2\text{Se}_3$  devices with the use of non-toxic and earth abundant transport materials and dopants.

Another important research direction is the characterization techniques used for the in-depth study of the defect chemistry and band alignment between the  $\text{Sb}_2\text{Se}_3$  and carrier transport layers. It is now evident that the identification of point defects in  $\text{Sb}_2\text{Se}_3$  is challenging due to their low concentrations, which often requires multiple analysis techniques such as electrical (XPS and HAXPES), optical (PL and photoconductivity), thermal (DLTS and temperature-dependent dark conductivity), and vibrational methods (infrared and Raman spectroscopy). Experimental control of defects concentrations is therefore achieved empirically due to the imperfect nature of experimental techniques to directly detect the level/species of defects in  $\text{Sb}_2\text{Se}_3$  thin films, which leads to the concentration and geometrical structures of defects being generally unpredictable. Hence, there is a significant gap remaining between the stages of understanding defect formation and the dynamics at the

atomic scale. This is therefore, a critical challenge in establishing a proper defect-structure-property relationship in functional  $\text{Sb}_2\text{Se}_3$  absorber in the near future.

It is critical to gain an in-depth understanding of defect formation processes and mechanisms to quantify and visualize defects at the atomic scale. In this regard, suitable development of experimental analysis methods assisted by theory and simulation tools is required. Consequently, computational studies like first-principal calculations and hybrid DFT are generally employed for a better understanding of experimental observations. However, with use of computational studies, identification of defects in the non-dilute limit (i.e., above a certain defect concentration), inter-dependency of defect properties, and analyzing of defect complexes with proper assessment of charge localization and charge transfer is significantly more challenging and computationally expensive. Despite these challenges, a combination of experimental and computational work should lead to an increased knowledge of defect chemistry. Hence, further progress in  $\text{Sb}_2\text{Se}_3$  thin films and related PV devices may greatly rely on the success in understanding, manipulating, and controlling their defects, which offers a versatile strategy for fabricating highly crystalline absorber films with preferred orientations.

## Conflicts of interest

The authors declare no conflict of interest.

## Acknowledgements

This work was supported by the Engineering and Physical Sciences Research Council [grant number EP/S023836/1].

## References

- 1 A. Mavlonov, T. Razykov, F. Raziq, J. Gan, J. Chantana, Y. Kawano, T. Nishimura, H. Wei, A. Zakutayev and T. Minemoto, *Sol. Energy*, 2020, **201**, 227–246.
- 2 M. Green, E. Dunlop, J. Hohl-Ebinger, M. Yoshita, N. Kopidakis and X. Hao, *Prog. Photovoltaics Res. Appl.*, 2021, **29**, 3–15.
- 3 R. Scheer and H.-W. Schock, *Chalcogenide photovoltaics: physics, technologies, and thin film devices*, John Wiley & Sons, 2011.
- 4 A. Zakutayev, *Curr. Opin. Green Sustainable Chem.*, 2017, **4**, 8–15.
- 5 J. Zhou, X. Xu, B. Duan, H. Wu, J. Shi, Y. Luo, D. Li and Q. Meng, *Nano Energy*, 2021, **89**, 106405.
- 6 T. D. Hobson, O. S. Hutter, N. Fleck, L. M. Daniels, J. D. Major, T. M. Ng and K. Durose, *Cryst. Growth Des.*, 2020, **20**, 2164–2173.
- 7 C. Chen, D. C. Bobela, Y. Yang, S. Lu, K. Zeng, C. Ge, B. Yang, L. Gao, Y. Zhao and M. C. Beard, *Front. Optoelectron.*, 2017, **10**, 18–30.
- 8 H. Lei, J. Chen, Z. Tan and G. Fang, *Sol. RRL*, 2019, **3**, 1900026.



- 9 O. S. Hutter, L. J. Phillips, K. Durose and J. D. Major, *Sol. Energy Mater. Sol. Cells*, 2018, **188**, 177–181.
- 10 Y. Zhou, M. Leng, Z. Xia, J. Zhong, H. Song, X. Liu, B. Yang, J. Zhang, J. Chen and K. Zhou, *Adv. Energy Mater.*, 2014, **4**, 1301846.
- 11 S. Ghosh, M. Moreira, C. Fantini and J. González, *Sol. Energy*, 2020, **211**, 613–621.
- 12 S. Chen, T. Liu, Z. Zheng, M. Ishaq, G. Liang, P. Fan, T. Chen and J. Tang, *J. Energy Chem.*, 2022, **67**, 508–523.
- 13 J. Tan, W. Yang, H. Lee, J. Park, K. Kim, O. S. Hutter, L. J. Phillips, S. Shim, J. Yun and Y. Park, *Appl. Catal., B*, 2021, **286**, 119890.
- 14 W. Yang, J. H. Kim, O. S. Hutter, L. J. Phillips, J. Tan, J. Park, H. Lee, J. D. Major, J. S. Lee and J. Moon, *Nat. Commun.*, 2020, **11**, 1–10.
- 15 W. Yang, J. Park, H.-C. Kwon, O. S. Hutter, L. J. Phillips, J. Tan, H. Lee, J. Lee, S. D. Tilley and J. D. Major, *Energy Environ. Sci.*, 2020, **13**, 4362–4370.
- 16 K. Zeng, D.-J. Xue and J. Tang, *Semicond. Sci. Technol.*, 2016, **31**, 063001.
- 17 X. Wang, Z. Li, S. R. Kavanagh, A. M. Ganose and A. Walsh, *Phys. Chem. Chem. Phys.*, 2022, **24**, 7195–7202.
- 18 Z. Li, X. Liang, G. Li, H. Liu, H. Zhang, J. Guo, J. Chen, K. Shen, X. San and W. Yu, *Nat. Commun.*, 2019, **10**, 1–9.
- 19 L. Wang, D.-B. Li, K. Li, C. Chen, H.-X. Deng, L. Gao, Y. Zhao, F. Jiang, L. Li and F. Huang, *Nat. Energy*, 2017, **2**, 1–9.
- 20 R. Kondrotas, J. Zhang, C. Wang and J. Tang, *Sol. Energy Mater. Sol. Cells*, 2019, **199**, 16–23.
- 21 Y. Zhou, L. Wang, S. Chen, S. Qin, X. Liu, J. Chen, D.-J. Xue, M. Luo, Y. Cao and Y. Cheng, *Nat. Photonics*, 2015, **9**, 409–415.
- 22 R. E. Williams, Q. M. Ramasse, K. P. McKenna, L. J. Phillips, P. J. Yates, O. S. Hutter, K. Durose, J. D. Major and B. G. Mendis, *ACS Appl. Mater. Interfaces*, 2020, **12**, 21730–21738.
- 23 G. Li, Z. Li, X. Liang, C. Guo, K. Shen and Y. Mai, *ACS Appl. Mater. Interfaces*, 2018, **11**, 828–834.
- 24 H. Shiel, O. S. Hutter, L. J. Phillips, J. E. Swallow, L. A. Jones, T. J. Featherstone, M. J. Smiles, P. K. Thakur, T.-L. Lee and V. R. Dhanak, *ACS Appl. Energy Mater.*, 2020, **3**, 11617–11626.
- 25 I. Gharibshahian, A. A. Orouji and S. Sharbati, *Sol. Energy Mater. Sol. Cells*, 2020, **212**, 110581.
- 26 B. Zhao, Z. Wan, J. Luo, C. Jia, X. Liu and R. Wang, *Appl. Mater. Today*, 2018, **12**, 191–197.
- 27 X. Wen, Y. He, C. Chen, X. Liu, B. Yang, M. Leng, H. Song, K. Zeng, D. Li and K. Li, *Sol. Energy Mater. Sol. Cells*, 2017, **172**, 74–81.
- 28 H. Guo, Z. Chen, X. Wang, Q. Cang, C. Ma, X. Jia, N. Yuan and J. Ding, *J. Mater. Chem. C*, 2019, **7**, 14350–14356.
- 29 C. Ou, K. Shen, Z. Li, H. Zhu, T. Huang and Y. Mai, *Sol. Energy Mater. Sol. Cells*, 2019, **194**, 47–53.
- 30 M. Huang, P. Xu, D. Han, J. Tang and S. Chen, *ACS Appl. Mater. Interfaces*, 2019, **11**, 15564–15572.
- 31 Y. Zhou, Y. Li, J. Luo, D. Li, X. Liu, C. Chen, H. Song, J. Ma, D.-J. Xue and B. Yang, *Appl. Phys. Lett.*, 2017, **111**, 013901.
- 32 Y. Ma, B. Tang, W. Lian, C. Wu, X. Wang, H. Ju, C. Zhu, F. Fan and T. Chen, *J. Mater. Chem. A*, 2020, **8**, 6510–6516.
- 33 X. Liu, C. Chen, L. Wang, J. Zhong, M. Luo, J. Chen, D. J. Xue, D. Li, Y. Zhou and J. Tang, *Prog. Photovoltaics Res. Appl.*, 2015, **23**, 1828–1836.
- 34 G.-X. Liang, Y.-D. Luo, S. Chen, R. Tang, Z.-H. Zheng, X.-J. Li, X.-S. Liu, Y.-K. Liu, Y.-F. Li and X.-Y. Chen, *Nano Energy*, 2020, **73**, 104806.
- 35 C. Chen, L. Wang, L. Gao, D. Nam, D. Li, K. Li, Y. Zhao, C. Ge, H. Cheong and H. Liu, *ACS Energy Lett.*, 2017, **2**, 2125–2132.
- 36 T. D. Hobson, L. J. Phillips, O. S. Hutter, K. Durose and J. D. Major, *Appl. Phys. Lett.*, 2020, **116**, 261101.
- 37 W. Shockley and H. J. Queisser, *J. Appl. Phys.*, 1961, **32**, 510–519.
- 38 L. J. Phillips, C. N. Savory, O. S. Hutter, P. J. Yates, H. Shiel, S. Mariotti, L. Bowen, M. Birkett, K. Durose and D. O. Scanlon, *IEEE J. Photovolt.*, 2018, **9**, 544–551.
- 39 X. Wen, C. Chen, S. Lu, K. Li, R. Kondrotas, Y. Zhao, W. Chen, L. Gao, C. Wang and J. Zhang, *Nat. Commun.*, 2018, **9**, 1–10.
- 40 J. Li, J. Huang, K. Li, Y. Zeng, Y. Zhang, K. Sun, C. Yan, C. Xue, C. Chen and T. Chen, *Sol. RRL*, 2021, **5**, 2000693.
- 41 R. Tang, Z.-H. Zheng, Z.-H. Su, X.-J. Li, Y.-D. Wei, X.-H. Zhang, Y.-Q. Fu, J.-T. Luo, P. Fan and G.-X. Liang, *Nano Energy*, 2019, **64**, 103929.
- 42 G.-X. Liang, X.-H. Zhang, H.-L. Ma, J.-G. Hu, B. Fan, Z.-K. Luo, Z.-H. Zheng, J.-T. Luo and P. Fan, *Sol. Energy Mater. Sol. Cells*, 2017, **160**, 257–262.
- 43 A. Shongalova, M. Correia, J. Teixeira, J. Leitao, J. Gonzalez, S. Ranjbar, S. Garud, B. Vermang, J. Cunha and P. Salomé, *Sol. Energy Mater. Sol. Cells*, 2018, **187**, 219–226.
- 44 D. Ren, S. Chen, M. Cathelinaud, G. Liang, H. Ma and X. Zhang, *ACS Appl. Mater. Interfaces*, 2020, **12**, 30572–30583.
- 45 D.-B. Li, X. Yin, C. R. Grice, L. Guan, Z. Song, C. Wang, C. Chen, K. Li, A. J. Cimaroli and R. A. Awni, *Nano Energy*, 2018, **49**, 346–353.
- 46 J. Kim, W. Yang, Y. Oh, H. Lee, S. Lee, H. Shin, J. Kim and J. Moon, *J. Mater. Chem. A*, 2017, **5**, 2180–2187.
- 47 Y. H. Kwon, Y. B. Kim, M. Jeong, H. W. Do, H. K. Cho and J. Y. Lee, *Sol. Energy Mater. Sol. Cells*, 2017, **172**, 11–17.
- 48 J. Ma, Y. Wang, Y. Wang, P. Peng, J. Lian, X. Duan, Z. Liu, X. Liu, Q. Chen and T. Kim, *CrystEngComm*, 2011, **13**, 2369–2374.
- 49 C. Karthik, R. J. Mehta, W. Jiang, E. Castillo, T. Borca-Tasciuc and G. Ramanath, *Appl. Phys. Lett.*, 2011, **99**, 103101.
- 50 S. Messina, M. Nair and P. Nair, *J. Electrochem. Soc.*, 2009, **156**, H327.
- 51 K. Bindu, M. Nair and P. Nair, *J. Electrochem. Soc.*, 2006, **153**, C526.
- 52 Y. C. Choi, T. N. Mandal, W. S. Yang, Y. H. Lee, S. H. Im, J. H. Noh and S. I. Seok, *Angew. Chem., Int. Ed.*, 2014, **126**, 1353–1357.
- 53 Z. Duan, X. Liang, Y. Feng, H. Ma, B. Liang, Y. Wang, S. Luo, S. Wang, R. E. Schropp and Y. Mai, *Adv. Mater.*, 2022, **34**, 2202969.



- 54 S. Rühle, *Sol. Energy*, 2016, **130**, 139–147.
- 55 C. Chen and J. Tang, *ACS Energy Lett.*, 2020, **5**, 2294–2304.
- 56 X. Wang, R. Tang, C. Jiang, W. Lian, H. Ju, G. Jiang, Z. Li, C. Zhu and T. Chen, *Adv. Energy Mater.*, 2020, **10**, 2002341.
- 57 J. Shi, Y. Wang, M. Yang, Y. Gu, W. An, Y. Men, J. Yang and Y. Rui, *Electrochim. Acta*, 2021, **376**, 138031.
- 58 Z. Cai and S. Chen, *J. Appl. Phys.*, 2020, **127**, 183101.
- 59 J. Dong, Y. Liu, Z. Wang and Y. Zhang, *Nano Sel.*, 2021, **2**, 1818–1848.
- 60 F. Ayala-Mató, O. Vigil-Galán, D. Seuret-Jiménez, M. Courel and S. Fernández, *Semicond. Sci. Technol.*, 2020, **36**, 015016.
- 61 W. Qiu, C. Zhang, S. Cheng, Q. Zheng, X. Yu, H. Jia and B. Wu, *J. Solid State Chem.*, 2019, **271**, 339–345.
- 62 R. Kondrotas, C. Chen and J. Tang, *Joule*, 2018, **2**, 857–878.
- 63 M. Leng, M. Luo, C. Chen, S. Qin, J. Chen, J. Zhong and J. Tang, *Appl. Phys. Lett.*, 2014, **105**, 083905.
- 64 S. Rijal, D.-B. Li, R. A. Awni, S. S. Bista, Z. Song and Y. Yan, *ACS Appl. Energy Mater.*, 2021, **4**, 4313–4318.
- 65 Z. Li, X. Chen, H. Zhu, J. Chen, Y. Guo, C. Zhang, W. Zhang, X. Niu and Y. Mai, *Sol. Energy Mater. Sol. Cells*, 2017, **161**, 190–196.
- 66 K. Shen, Y. Zhang, X. Wang, C. Ou, F. Guo, H. Zhu, C. Liu, Y. Gao, R. E. Schropp and Z. Li, *Adv. Sci.*, 2020, **7**, 2001013.
- 67 X. Liu, J. Chen, M. Luo, M. Leng, Z. Xia, Y. Zhou, S. Qin, D.-J. Xue, L. Lv and H. Huang, *ACS Appl. Mater. Interfaces*, 2014, **6**, 10687–10695.
- 68 S. Chen, Z. Zheng, M. Cathelinaud, H. Ma, X. Qiao, Z. Su, P. Fan, G. Liang, X. Fan and X. Zhang, *Sol. Energy Mater. Sol. Cells*, 2019, **203**, 110154.
- 69 H.-j. Wu, P.-c. Lee, F.-y. Chiu, S.-w. Chen and Y.-y. Chen, *J. Mater. Chem. C*, 2015, **3**, 10488–10493.
- 70 D. Ren, X. Luo, S. Chen, Z. Zheng, M. Cathelinaud, G. Liang, H. Ma, X. Qiao, X. Fan and X. Zhang, *Nanomaterials*, 2020, **10**, 1358.
- 71 R. S. Rahman, K. Asokan and M. Zulfeqar, *J. Phys. Chem. C*, 2022, **126**, 6065–6074.
- 72 Y. Wang, J. Li, Y. Chen, J. Zhou, J. Zhang, W. Mao, S. Zheng, Y. Pan, Y. Liu and K. Dai, *Appl. Opt.*, 2020, **59**, 948–954.
- 73 J. S. Park, S. Kim, Z. Xie and A. Walsh, *Nat. Rev. Mater.*, 2018, **3**, 194–210.
- 74 X. Zhang, M. E. Turiansky, J.-X. Shen and C. G. Van de Walle, *Phys. Rev. B*, 2020, **101**, 140101.
- 75 C. N. Savory and D. O. Scanlon, *J. Mater. Chem. A*, 2019, **7**, 10739–10744.
- 76 A. Stolaroff, A. Lecomte, O. Rubel, S. Jovic, X. Zhang, C. Latouche and X. Roquefelte, *ACS Appl. Energy Mater.*, 2020, **3**, 2496–2509.
- 77 M. A. Tumelero, R. Faccio and A. A. Pasa, *J. Phys. Chem. C*, 2016, **120**, 1390–1399.
- 78 X. Liu, X. Xiao, Y. Yang, D. J. Xue, D. B. Li, C. Chen, S. Lu, L. Gao, Y. He and M. C. Beard, *Prog. Photovoltaics Res. Appl.*, 2017, **25**, 861–870.
- 79 K. Wang, C. Chen, H. Liao, S. Wang, J. Tang, M. C. Beard and Y. Yang, *J. Phys. Chem. Lett.*, 2019, **10**, 4881–4887.
- 80 N. Cifuentes, S. Ghosh, A. Shongolova, M. Correia, P. Salomé, P. Fernandes, S. Ranjbar, S. Garud, B. Vermang and G. Ribeiro, *J. Phys. Chem. C*, 2020, **124**, 7677–7682.
- 81 M. Grossberg, O. Volobujeva, A. Penezko, R. Kaupmees, T. Raadik and J. Krustok, *J. Alloys Compd.*, 2020, **817**, 152716.
- 82 Z. Bi, X. Rodríguez-Martínez, C. Aranda, E. Pascual-San-José, A. R. Goñi, M. Campoy-Quiles, X. Xu and A. Guerrero, *J. Mater. Chem. A*, 2018, **6**, 19085–19093.
- 83 J. Du, R. Singh, I. Fedin, A. S. Fuhr and V. I. Klimov, *Nat. Energy*, 2020, **5**, 409–417.
- 84 M. Huang, Z. Cai, S. Wang, X. G. Gong, S. H. Wei and S. Chen, *Small*, 2021, **17**, 2102429.
- 85 M. Wang and B. Duan, *Encyclopedia of Biomedical Engineering*, Elsevier, 2019, pp. 135–152.
- 86 J. C. González, H. Limborço, R. Ribeiro-Andrade, B. C. Silva and K. Krambrock, *Adv. Electron. Mater.*, 2022, **8**, 2100985.
- 87 N. Spalatu, R. Krautmann, A. Katerski, E. Karber, R. Josepson, J. Hiie, I. O. Acik and M. Krunks, *Sol. Energy Mater. Sol. Cells*, 2021, **225**, 111045.
- 88 K. Nishidate, T. Sato, Y. Matsukura, M. Baba, M. Hasegawa and T. Sasaki, *Phys. Rev. B: Condens. Matter Mater. Phys.*, 2006, **74**, 035210.
- 89 S.-H. Wei and S. Zhang, *Phys. Rev. B: Condens. Matter Mater. Phys.*, 2002, **66**, 155211.
- 90 X. Hu, J. Tao, G. Weng, J. Jiang, S. Chen, Z. Zhu and J. Chu, *Sol. Energy Mater. Sol. Cells*, 2018, **186**, 324–329.
- 91 L. Gilbert, B. Van Pelt and C. Wood, *J. Phys. Chem. Solids*, 1974, **35**, 1629–1632.
- 92 X. Hu, J. Tao, Y. Wang, J. Xue, G. Weng, C. Zhang, S. Chen, Z. Zhu and J. Chu, *Appl. Mater. Today*, 2019, **16**, 367–374.
- 93 J. Krustok, H. Collan, K. Hjelt, J. Mäddasson and V. Valdna, *J. Lumin.*, 1997, **72**, 103–105.
- 94 X. Hu, J. Tao, S. Chen, J. Xue, G. Weng, Z. Hu, J. Jiang, S. Chen, Z. Zhu and J. Chu, *Sol. Energy Mater. Sol. Cells*, 2018, **187**, 170–175.
- 95 J. Tao, X. Hu, Y. Guo, J. Hong, K. Li, J. Jiang, S. Chen, C. Jing, F. Yue and P. Yang, *Nano Energy*, 2019, **60**, 802–809.
- 96 Y.-D. Luo, R. Tang, S. Chen, J.-G. Hu, Y.-K. Liu, Y.-F. Li, X.-S. Liu, Z.-H. Zheng, Z.-H. Su and X.-F. Ma, *Chem. Eng. J.*, 2020, **393**, 124599.
- 97 G. Coletti, P. C. Bronsveld, G. Hahn, W. Warta, D. Macdonald, B. Ceccaroli, K. Wambach, N. Le Quang and J. M. Fernandez, *Adv. Funct. Mater.*, 2011, **21**, 879–890.
- 98 A. Peaker, V. Markevich, B. Hamilton, G. Parada, A. Dudas, A. Pap, E. Don, B. Lim, J. Schmidt and L. Yu, *Journal*, 2012, **209**, 1884–1893.
- 99 S. Chen, X. Qiao, Z. Zheng, M. Cathelinaud, H. Ma, X. Fan and X. Zhang, *J. Mater. Chem. C*, 2018, **6**, 6465–6470.
- 100 Z. Cai, C.-M. Dai and S. Chen, *Sol. RRL*, 2020, **4**, 1900503.
- 101 Y. Li, Y. Zhou, J. Luo, W. Chen, B. Yang, X. Wen, S. Lu, C. Chen, K. Zeng and H. Song, *RSC Adv.*, 2016, **6**, 87288–87293.
- 102 A. Alemi, Y. Hanifehpour, S. W. Joo, B.-K. Min and T. H. Oh, *J. Nanomater.*, 2012, **2012**, 983150.



- 103 A. Alemi, Y. Hanifehpour, S. W. Joo, A. Khandar, A. Morsali and B.-K. Min, *Phys. B*, 2012, **407**, 38–43.
- 104 A. Alemi, Y. Hanifehpour, S. W. Joo and B.-K. Min, *Colloids Surf., A*, 2011, **390**, 142–148.
- 105 C. Guo, X. Liang, T. Liu, Y. Liu, L. Yang, W. Lai, R. E. Schropp, D. Song, Y. Mai and Z. Li, *Sol. RRL*, 2020, **4**, 2000054.
- 106 Y. Li, Y. Zhou, Y. Zhu, C. Chen, J. Luo, J. Ma, B. Yang, X. Wang, Z. Xia and J. Tang, *Appl. Phys. Lett.*, 2016, **109**, 232104.
- 107 C. Chen, K. Li, S. Chen, L. Wang, S. Lu, Y. Liu, D. Li, H. Song and J. Tang, *ACS Energy Lett.*, 2018, **3**, 2335–2341.
- 108 T. D. Hobson, L. J. Phillips, O. S. Hutter, H. Shiel, J. E. Swallow, C. N. Savory, P. K. Nayak, S. Mariotti, B. Das and L. Bowen, *Chem. Mater.*, 2020, **32**, 2621–2630.
- 109 C. Chen, Y. Zhao, S. Lu, K. Li, Y. Li, B. Yang, W. Chen, L. Wang, D. Li and H. Deng, *Adv. Energy Mater.*, 2017, **7**, 1700866.
- 110 X. Wang, R. Tang, Y. Yin, H. Ju, C. Zhu and T. Chen, *Sol. Energy Mater. Sol. Cells*, 2019, **189**, 5–10.
- 111 S. Lu, H. Ding, J. Hu, Y. Liu, J. Zhu, R. Kondrotas, C. Chen and J. Tang, *Appl. Phys. Lett.*, 2020, **116**, 241602.
- 112 S. Siol, P. Schulz, M. Young, K. A. Borup, G. Teeter and A. Zakutayev, *Adv. Mater. Interfaces*, 2016, **3**, 1600755.
- 113 K. Li, C. Chen, S. Lu, C. Wang, S. Wang, Y. Lu and J. Tang, *Adv. Mater.*, 2019, **31**, 1903914.
- 114 L. Zhang, Y. Li, C. Li, Q. Chen, Z. Zhen, X. Jiang, M. Zhong, F. Zhang and H. Zhu, *ACS Nano*, 2017, **11**, 12753–12763.
- 115 K. Akimoto, H. Okuyama, M. Ikeda and Y. Mori, *J. Cryst. Grow.*, 1992, **117**, 420–423.
- 116 L. Guo, B. Zhang, S. Ranjit, J. Wall, S. Saurav, A. J. Hauser, G. Xing, L. Li, X. Qian and F. Yan, *Sol. RRL*, 2019, **3**, 1900225.
- 117 L. Wang, M. Luo, S. Qin, X. Liu, J. Chen, B. Yang, M. Leng, D.-J. Xue, Y. Zhou and L. Gao, *Appl. Phys. Lett.*, 2015, **107**, 143902.
- 118 L. Guo, B. Zhang, S. Li, A. Montgomery, L. Li, G. Xing, Q. Zhang, X. Qian and F. Yan, *Mater. Today Phys.*, 2019, **10**, 100125.
- 119 S. Rijal, D. B. Li, R. A. Awni, C. Xiao, S. S. Bista, M. K. Jamarkattel, M. J. Heben, C. S. Jiang, M. Al-Jassim and Z. Song, *Adv. Funct. Mater.*, 2022, **32**, 2110032.
- 120 K. Szendrei, W. Gomulya, M. Yarema, W. Heiss and M. A. Loi, *Appl. Phys. Lett.*, 2010, **97**, 203501.
- 121 J. Tao, X. Hu, J. Xue, Y. Wang, G. Weng, S. Chen, Z. Zhu and J. Chu, *Sol. Energy Mater. Sol. Cells*, 2019, **197**, 1–6.
- 122 K. Yang, B. Li and G. Zeng, *Sol. Energy Mater. Sol. Cells*, 2020, **208**, 110381.
- 123 Z. Zhang, M. Hu, T. Jia, J. Du, C. Chen, C. Wang, Z. Liu, T. Shi, J. Tang and Y. Leng, *ACS Energy Lett.*, 2021, **6**, 1740–1748.
- 124 W. Yang, S. Lee, H.-C. Kwon, J. Tan, H. Lee, J. Park, Y. Oh, H. Choi and J. Moon, *ACS Nano*, 2018, **12**, 11088–11097.
- 125 P. Sommeling, B. C. O'Regan, R. Haswell, H. Smit, N. Bakker, J. Smits, J. M. Kroon and J. Van Roosmalen, *J. Phys. Chem. B*, 2006, **110**, 19191–19197.
- 126 K. Li, R. Kondrotas, C. Chen, S. Lu, X. Wen, D. Li, J. Luo, Y. Zhao and J. Tang, *Sol. Energy*, 2018, **167**, 10–17.
- 127 J. Zhou, X. Zhang, H. Chen, Z. Tang, D. Meng, K. Chi, Y. Cai, G. Song, Y. Cao and Z. Hu, *Appl. Surf. Sci.*, 2020, **534**, 147632.
- 128 S. Lu, Y. Zhao, C. Chen, Y. Zhou, D. Li, K. Li, W. Chen, X. Wen, C. Wang and R. Kondrotas, *Adv. Electron. Mater.*, 2018, **4**, 1700329.
- 129 J. Zhang, R. Kondrotas, S. Lu, C. Wang, C. Chen and J. Tang, *Sol. Energy*, 2019, **182**, 96–101.
- 130 C. Liu, K. Shen, D. Lin, Y. Cao, S. Qiu, J. Zheng, F. Bao, Y. Gao, H. Zhu and Z. Li, *ACS Appl. Mater. Interfaces*, 2020, **12**, 38397–38405.
- 131 Y. Ma, Y. Yin, G. Li, W. Lian, J. Zhang, R. Tang, H. Ju and T. Chen, *Chem. Commun.*, 2020, **56**, 15173–15176.
- 132 L. J. Phillips, P. Yates, O. S. Hutter, T. Baines, L. Bowen, K. Durose and J. D. Major, Close-spaced sublimation for Sb<sub>2</sub>Se<sub>3</sub> solar cells, *2017 IEEE 44th Photovoltaic Specialist Conference (PVSC)*, IEEE, 2017, pp. 1445–1448.
- 133 A. E. R. Mohamed and S. Rohani, *Energy Environ. Sci.*, 2011, **4**, 1065–1086.
- 134 M. Asaduzzaman, M. Hasan and A. N. Bahar, *SpringerPlus*, 2016, **5**, 1–8.
- 135 D.-F. Li, M. Luo, B.-L. Li, C.-B. Wu, B. Deng and H.-N. Dong, *Adv. Condens. Matter Phys.*, 2013, **2013**, 739078.
- 136 M. Grundmann, *Physics of semiconductors*, Springer, 2010.
- 137 G. Altamura, M. Wang and K.-L. Choy, *Sci. Rep.*, 2016, **6**, 1–9.
- 138 C. Yang, Y. Wang, S. Li, D. Wan and F. Huang, *J. Mater. Sci.*, 2012, **47**, 7085–7089.
- 139 M. B. Costa, F. W. de Souza Lucas and L. H. Mascaro, *J. Solid State Electrochem.*, 2018, **22**, 1557–1562.
- 140 P. Myagmarsereejid, M. Ingram, M. Batmunkh and Y. L. Zhong, *Small*, 2021, **17**, 2100241.
- 141 A. Walsh, J. L. Da Silva and S.-H. Wei, *Phys. Rev. B: Condens. Matter Mater. Phys.*, 2008, **78**, 075211.
- 142 Z. M. Gibbs, A. LaLonde and G. J. Snyder, *New J. Phys.*, 2013, **15**, 075020.
- 143 W.-H. Li, M. Li, Y.-J. Hu, C.-H. Cheng, Z.-M. Kan, D. Yu, J. Leng, S. Jin and S. Cong, *Appl. Phys. Lett.*, 2021, **118**, 093903.
- 144 J. Major, R. Treharne, L. Phillips and K. Durose, *Nature*, 2014, **511**, 334–337.
- 145 Y. Ma, B. Tang, W. Lian, C. Wu, X. Wang, H. Ju, C. Zhu, F. Fan and T. Chen, *J. Mater. Chem. A*, 2020, **8**, 6510–6516.
- 146 A. Alemi, Y. Hanifehpour, S. W. Joo, A. Khandar, A. Morsali and B.-K. Min, *Phys. B*, 2011, **406**, 2801–2806.
- 147 A. Alemi, Y. Hanifehpour, S. W. Joo and B.-K. Min, *Phys. B*, 2011, **406**, 3831–3835.
- 148 Y. Hanifehpour, S. W. Joo and B.-K. Min, *Nanoscale Res. Lett.*, 2013, **8**, 1–8.
- 149 J. Li, B. Wang, F. Liu, J. Yang, J. Li, J. Liu, M. Jia, Y. Lai and Y. Liu, *Electrochim. Acta*, 2011, **56**, 8597–8602.
- 150 M. Kamruzzaman, C. Liu, A. Farid Ul Islam and J. Zapien, *Semiconductors*, 2017, **51**, 1615–1624.
- 151 Y. Lai, Z. Chen, C. Han, L. Jiang, F. Liu, J. Li and Y. Liu, *Appl. Surf. Sci.*, 2012, **261**, 510–514.



- 152 C. Ma, H. Guo, X. Wang, Z. Chen, Q. Cang, X. Jia, Y. Li, N. Yuan and J. Ding, *Sol. Energy*, 2019, **193**, 275–282.
- 153 S. Li, H. Shen, J. Chen, Y. Jiang, L. Sun, A. Raza and Y. Xu, *J. Mater. Sci.: Mater. Electron.*, 2019, **30**, 19871–19879.
- 154 S. Rijal, Z. Song, D.-B. Li, S. S. Bista and Y. Yan, Optimizing the Selenization of  $\text{Sb}_2\text{Se}_3$  Absorbers to Improve the Film Quality and Solar Cell Performances, *2021 IEEE 48th Photovoltaic Specialists Conference (PVSC)*, IEEE, 2021, pp. 1148–1151.
- 155 S. Yao, J. Wang, J. Cheng, L. Fu, F. Xie, Y. Zhang and L. Li, *ACS Appl. Mater. Interfaces*, 2020, **12**, 24112–24124.
- 156 P. Vidal-Fuentes, M. Placidi, Y. Sánchez, I. Becerril-Romero, J. Andrade-Arvizu, Z. Jehl, A. Pérez-Rodríguez, V. Izquierdo-Roca and E. Saucedo, *Sol. RRL*, 2020, **4**, 2000141.
- 157 H. Guo, C. Zhao, Y. Xing, H. Tian, D. Yan, S. Zhang, X. Jia, J. Qiu, N. Yuan and J. Ding, *J. Phys. Chem. Lett.*, 2021, **12**, 12352–12359.
- 158 W. Wang, Z. Cao, L. Wu, G. Chen, J. Ao, J. Luo and Y. Zhang, *ACS Appl. Energy Mater.*, 2022, **5**, 2531–2541.
- 159 H. Shiel, O. S. Hutter, L. J. Phillips, M. Al Turkestani, V. R. Dhanak, T. D. Veal, K. Durose and J. D. Major, *J. Phys.: Energy*, 2019, **1**, 045001.
- 160 Y.-S. Tyan and E. Perez-Alburne, Efficient thin-film CdS/CdTe solar cells, *Conf. Rec. IEEE Photovoltaic Spec. Conf.*, 1982.
- 161 N. Fleck, O. S. Hutter, L. J. Phillips, H. Shiel, T. D. Hobson, V. R. Dhanak, T. D. Veal, F. Jäckel, K. Durose and J. D. Major, *ACS Appl. Mater. Interfaces*, 2020, **12**, 52595–52602.
- 162 C. Wang, S. Lu, S. Li, S. Wang, X. Lin, J. Zhang, R. Kondrotas, K. Li, C. Chen and J. Tang, *Nano Energy*, 2020, **71**, 104577.

